

The habitat of the nascent Chicxulub crater

T. J. Bralower¹, J. Cosmidis¹, M. S. Fantle¹, C. M. Lowery², B. H. Passey³, S. P. S. Gulick², J. V. Morgan⁴, V. Vajda⁵, M. T. Whalen⁶, A. Wittmann⁷, N. Artemieva⁸, K. Farley⁹, S. Goderis¹⁰, E. Hajek¹, P. J. Heaney¹, D. A. Kring¹¹, S. L. Lyons¹, C. Rasmussen², E. Sibert¹², F. J. Rodríguez Tovar¹³, G. Turner-Walker¹⁴, J. C. Zachos¹⁵, J. Carte¹, S. A. Chen¹, C. Cockell¹⁶, M. Coolen¹⁷, K. H. Freeman¹, J. Garber¹, M. Gonzalez¹, J. L. Gray¹⁸, K. Grice¹⁷, H. L. Jones¹, B. Schaefer¹⁷, J. Smit¹⁹, S. M. Tikoo²⁰

¹Department of Geosciences, Pennsylvania State University, University Park, PA, 16802, USA

²Institute for Geophysics, Jackson School of Geosciences, University of Texas at Austin, Austin, TX 78758, USA

³Department of Earth and Environmental Sciences, University of Michigan, Ann Arbor, MI 48109-1005, USA

⁴Department of Earth Science and Engineering, Imperial College London, UK

⁵Department of Palaeobiology, Swedish Museum of Natural History, Stockholm, Sweden

⁶Geophysical Institute, University of Alaska, Fairbanks, AK 99775, USA

⁷Eyring Materials Center, Arizona State University Tempe, AZ 85287-8301, USA

⁸Planetary Science Institute, Tucson, AZ, USA

⁹Division of Geological and Planetary Sciences, California Institute of Technology, Pasadena, CA 91125, USA

¹⁰Department of Chemistry, Vrije Universiteit Brussel, BE-1050 Brussels, Belgium

¹¹Lunar and Planetary Institute, 3600 Bay Area Blvd., Houston, TX 77058-1113, USA

¹²Department of Earth and Planetary Sciences, Yale University, New Haven, CT, 06520, USA

¹³Departamento de Estratigrafía y Paleontología, Facultad de Ciencias, Universidad de Granada, Granada 18002, Spain

¹⁴Graduate School of Cultural Heritage Conservation, National Yunlin University of Science and Technology, 640 Yunlin, Taiwan

¹⁵Earth and Planetary Sciences, University of California Santa Cruz, 1156 High Street, Santa Cruz, CA 95064, USA

42

43 ¹⁶School of Physics and Astronomy, University of Edinburgh, Edinburgh, EH9 3FD, UK

44

45 ¹⁷Organic and Isotope Geochemistry Centre, The Institute for Geoscience Research, School
46 of Earth and Planetary Science, Curtin University, Perth, WA, Australia

47

48 ¹⁸Materials Research Institute, Pennsylvania State University, University Park, PA, 16802,
49 USA

50

51 ¹⁹Department of Geology and Geochemistry, VU University Amsterdam 1081HV
52 Amsterdam, The Netherlands

53

54 ²⁰Department of Geophysics, Stanford University, Stanford, CA 94305, USA

55

56

57 Corresponding author: Timothy J. Bralower (bralower@psu.edu)

58

59

60

61 **Key Points:**

- 62 ▪ Sediments derived from decarbonation of the Chicxulub impact target were
63 deposited by tsunami and seiche waves over months to years followed by a layer
64 with atmospheric fallout
- 65
- 66 ▪ Temperatures in the ocean above the hotter regions of the crater were in excess of
67 70 °C, with heat likely derived from the central impact melt pool
- 68
- 69 ▪ Cooler regions within the crater basin became habitats soon after impact with
70 diverse life ranging from microbes to marine arthropods, and possibly fish

71 Abstract

72 An expanded sedimentary section provides an opportunity to elucidate conditions in the
73 nascent Chicxulub crater during the hours to millennia after the Cretaceous-Paleogene (K-Pg)
74 boundary impact. The sediments were deposited by tsunami followed by seiche waves as
75 energy in the crater declined, culminating in a thin hemipelagic marlstone unit that contains
76 atmospheric fallout. Seiche deposits are predominantly composed of calcite formed by
77 decarbonation of the target limestone during impact followed by carbonation in the water
78 column. Temperatures recorded by clumped isotopes of these carbonates are in excess of 70
79 °C, with heat likely derived from the central impact melt pool. Yet, despite the turbidity and
80 heat, waters within the nascent crater basin soon became a viable habitat for a remarkably
81 diverse cross-section of the food chain. The earliest seiche layers deposited with days or weeks
82 of the impact contain earliest Danian nannoplankton and dinocyst survivors. The hemipelagic
83 marlstone representing the subsequent years to a few millennia contains a nearly monogeneric
84 calcareous dinoflagellate resting cyst assemblage suggesting deteriorating environmental
85 conditions, with one interpretation involving low light levels in the impact aftermath. At the
86 same horizon, microbial fossils indicate a thriving bacterial community and unique phosphatic
87 fossils including appendages of pelagic crustaceans, coprolites and bacteria-tunneled fish
88 bone, suggesting that this rapid recovery of the base of the food chain may have supported the
89 survival of larger, higher trophic-level organisms. The extraordinarily diverse fossil
90 assemblage indicates that the crater was a unique habitat in the immediate impact aftermath,
91 possibly as a result of heat and nutrients supplied by hydrothermal activity.

92

93

94 Plain Language Summary

95

96 The newly formed Chicxulub crater was rapidly filled by seawater then disturbed by tsunami
97 and seiche waves. Sedimentary layers deposited as wave energy declined provide a unique
98 window into the environment of the nascent crater in the months and years to millennia after
99 the impact. Geochemical data show temperatures in hotter regions of the crater in excess of 70
100 °C for the first few years with heat derived from the underlying melt sheet via hydrothermal
101 circulation. Cooler regions of the crater became habitats soon after impact with a suite of fossils
102 indicating diverse life on the seafloor and sea surface, ranging from microbes to marine
103 arthropods, and possibly fish. We suggest that this community was sustained by nutrients and
104 heat from the hydrothermal system. The rapid early recovery in the Chicxulub crater and ocean
105 above demonstrates the resiliency of life under extraordinarily harsh conditions, which has
106 important ramifications for early life on Earth and life on other planets.

107

108

109 **1. Introduction**

110 In one of the most rapid geomorphic events in Earth history, the 200 km diameter Chicxulub
111 crater formed in minutes to hours^{1,2} and caused major environmental upheaval that led to mass
112 extinction marked by the Cretaceous-Paleogene (K-Pg) boundary^{3,4 5}. The shallow sea as well
113 as the carbonate and evaporite rocks at the location of impact (i.e., the target rocks), amplified
114 the environmental effects of the event. Prolonged impact winter, cessation of photosynthesis,
115 and, perhaps acid rain resulting from release of SO₂ from evaporite sulfates^{6-9 10-14}, were likely
116 major killing mechanisms on land and in the oceans. These effects may have been enhanced
117 by soot released by wildfires^{15,16} and combusted target rock hydrocarbons^{17 18}, and carbonate

118 dust¹⁹, though this latter material has not been identified in boundary deposits. The impact
119 occurred between eruption of Deccan Traps lavas that were unrelated to the mass extinction²⁰.
120 Once formed, impact craters such as Chicxulub can provide unique habitats for life^{2,21}, a
121 function that may also have been in operation early in Earth history². Hydrothermal systems
122 initiated by impact have the potential to release nutrients and energy for microbial activity²²⁻
123 ²⁵, and the presence of hydrothermal minerals within the crater's peak ring confirm that hot
124 fluids circulated in these rocks after crater formation²⁶. These impact lithologies today host
125 diverse microbial communities shaped by the impact event²⁷. However, to this point there has
126 been little exploration of the connection between hydrothermal activity and local marine life
127 in the aftermath of an impact^{26,28}.

128

129 The geological record of the Chicxulub crater offers clues regarding the dynamic processes
130 that occurred in the immediate aftermath of the impact and affected the habitability of the
131 nascent crater. Immediately after impact, a ~200-km wide impact basin was formed with an
132 internal 80- to 90-km-diameter topographic peak ring surrounding a central basin containing
133 a thick suevite (i.e., melt-bearing impact breccia) layer above an impact melt sheet²².
134 Heterogeneity in topography, structure and nature of the near-surface rocks led to considerable
135 variability in heat and fluid flow, which would have affected the chemistry of the initial waters
136 that entered the crater. While Chicxulub has been the target of extensive geophysical
137 exploration in the past^{29 30}, existing boreholes were either only spot cored or located on the
138 inner ring crater slope where accommodation space was limited and the boundary sequence is
139 condensed and incomplete^{31 32}. The Yaxcopoil-1 (YAX-1) core, drilled adjacent to the inner
140 ring of the crater contains evidence for hydrothermal circulation in impact breccias^{33 34 35} and

141 overlying Paleogene limestones that suggests that hydrothermal activity persisted for hundreds
142 of thousands of years after the impact³⁶. However, repeated mass wasting events at YAX-1
143 from the adjacent inner crater rim obscure the sedimentary record of the years after the impact
144^{37,38}, limiting our ability to document the history of the recovery of life and of hydrothermal
145 activity.

146

147 International Ocean Discovery Program-International Continental Scientific Drilling Program
148 (IODP-ICDP) Expedition 364 drilled into the Chicxulub peak ring at Site M0077³⁹. The site
149 was located in a depression on top of the peak ring, providing the accommodation space for
150 the accumulation of a remarkable boundary sequence. Site M0077 recovered 587 m of felsic
151 basement rocks overlain by 130 m of suevite. The lowermost suevite was emplaced as the
152 central uplift collapsed to form the peak ring, and suevite deposition continued during ocean
153 resurge, seiche (internal to the crater) and tsunami waves¹³. Site M0077 granitoid rocks and
154 suevites show mineralogical and paleomagnetic evidence of long-lasting hydrothermal
155 circulation^{26,39}. The uppermost 8.5 m [617.33-625.85 meters below sea floor (mbsf)] of these
156 deposits, largely very fine-grained, layered suevite that was laid down by a succession of
157 seiches, are capped by a coarser grained, cross-bedded tsunami-deposited unit. The suevite
158 (Unit 2A of Gulick et al., 2017⁴⁰) grades into a 75 cm generally upward-fining, brown, fine-
159 grained limestone termed the “transitional unit”⁴¹ (Unit 1G of Gulick et al., 2017⁴⁰; 617.33 to
160 616.58 mbsf), which was deposited by settling, tsunami, and seiches⁴². This unit is in turn
161 overlain by a 3-cm thick green marlstone⁴⁰; 616.58 to 616.55 mbsf (here termed Unit 1G/1F
162 transition) that grades into pelagic white limestone (Unit 1F of Gulick et al., 2017⁴⁰) (Figure
163 1). The lower 52 cm of the transitional unit contains mm-scale laminations and graded beds,

164 and the upper 19 cm also contains cross beds and hummocky cross stratification which signify
165 deposition by bottom currents associated with residual seiches within the crater⁴². The fine silt
166 and clay grain size of the transitional unit suggests that the majority of sediment was delivered
167 by resuspension and settling. A 20-cm interval of soft-sediment deformation occurs in the
168 middle of the transitional unit, and the upper ~15 cm of the unit is burrowed⁴¹. The transitional
169 unit contains clay and pyrite, and is bounded by two intervals enriched in charcoal, which
170 likely settled from the ocean surface transported by either wave energy or through the
171 atmosphere¹³. The occurrence of charcoal and evidence for high-energy transport suggests that
172 the majority of the transitional unit was deposited very rapidly within days to, at most, years
173 after the impact. This interpretation was originally based on Helium-3 measurements and
174 Stokes Law calculations⁴¹, and is confirmed by enrichment of Ir in the uppermost transitional
175 unit and green marlstone (between 616.60 and 616.55 mbsf) that indicates settling of
176 meteoritic material, likely within a few years of the impact⁴³. Site M0077 thus represents the
177 most expanded post-impact drill core record yet recovered of the immediate aftermath of the
178 Chicxulub impact event¹³.

179

180 The transitional unit contains rare calcareous nannofossils and common planktic foraminifera,
181 with survivor species of the latter group becoming more common upsection, indicating the
182 appearance of pelagic life in the crater at least by the time burrows indicate a benthic infauna,
183 less than a few years after impact⁴¹. The majority of the unit is composed of microcrystalline
184 calcite, also known as micrite. Scanning electron microscopy (SEM) reveals rare microcrystals
185 that have been interpreted as microbial in origin⁴⁴. The bulk of the micrite was likely derived
186 from CaO via thermal decarbonation (emission of CO₂) of sedimentary target-rocks during

187 impact followed by carbonation (backreaction via addition of CO₂) to CaCO₃, as suggested for
188 select carbonate particles found at other K-Pg sites^{45 44,46}. However, the mechanics of
189 carbonation are not well understood and it is unclear whether it took place in the late stages of
190 impact plume expansion, during the resurgence of ocean waters back into the crater, in the water
191 column after crater flooding, or during burial in the months to years that the transitional unit
192 was formed.

193

194 Rapid deposition of the transitional unit offers the potential to determine the effects of reduced
195 photosynthesis, impact winter and hydrothermal activity on life at the dawn of the Cenozoic
196 era. Yet the proxy record can only be evaluated once the formation of micrite is constrained.
197 Moreover, interpretation of the fossil record is complicated by the high-energy depositional
198 environment in which reworking of microscopic plankton tests is common⁴¹. Here we explore
199 the origin of the materials in the transitional unit and green marlstone on top of Chicxulub's
200 peak ring at Site M0077 and probe evidence for recovery of the food chain in the early crater
201 in the first months to thousands of years of the Cenozoic. We use optical microscopy, scanning
202 and transmission electron microscopy (SEM and TEM), clumped, strontium, and carbon and
203 oxygen stable isotopes (see Supplemental Materials for Methods), and current age models to
204 constrain conditions in the early crater, and compare them to the fossil evidence for the
205 recovery of life at ground zero. Our results illustrate that, despite harsh post-impact conditions,
206 the incipient crater became home to the most diverse post-impact marine assemblage
207 documented to date. This illustrates that craters can be viable habitats for life even in the
208 immediate aftermath of impact.

209

210 **2. Results**

211

212 2.1 Character of micrite

213 Dramatic changes in the size and shape of micrite particles from the upper suevite through the
214 transitional unit into the green marlstone are observed via backscatter electron microscopy
215 (BSE) (Figure 1; Supplemental Materials Figure 1). Abundant micrite is found in the topmost
216 suevite (617.54 to 617.43 mbsf) where it is generally angular in shape. In the topmost suevite
217 (617.43 to 617.33 mbsf) and lowermost transitional unit (617.33 to 617.30 mbsf), micrite
218 particles are generally rounded to subrounded, flattened, and 10 to 150 μm in size, and samples
219 have a low porosity and a high clay content, as observed in BSE images (Figure 1, Pl. 7-11;
220 Supplemental Materials Figure 1, Pl. 6-10). The compacted nature of rounded micrite particles
221 in this interval (Figure 1, Pl. 8-10; Supplemental Materials Figure 1, Pl. 6-9) indicates
222 alteration by pressure solution during burial. In the remainder of the transitional unit, between
223 617.33 and 616.58 mbsf, micrite particles are generally highly irregular in size, and smaller,
224 between 0.5 and 20 μm , more angular in shape, densely packed but rarely compressed, and
225 with a lower clay content (Figure 1, Pl. 3-6; Supplemental Materials Figure 1, Pl. 2-5). Calcite
226 in the green marlstone (616.58 to 616.54 mbsf) is composed of miniscule planktic foraminifera
227 (generally 20 to 40 μm) and very fine micrite (<0.5 to 2 μm ; Figure 1, Pl. 1, 2; Supplemental
228 Materials Figure 1, Pl. 1). Rare silicate melt particles are also observed (Figure 1; Pl. 1;
229 Supplemental Materials Figure 2; Pl. 1-5) and clay content increases in this interval. The fine
230 micrite resembles micrite in the transitional unit under cross-polarized light and is distinct
231 from micrite in the overlying white limestone.

232

233 2.2 Character of charcoal and pyrite

234 Charcoal is generally rare throughout the transitional unit but is common in two intervals
235 (Figure 2): (1) at the base of the transitional unit and the underlying cross-bedded sand-sized
236 interval at the top of the uppermost suevite (617.34 to 617.27 mbsf); and (2) at the top of the
237 transitional unit, and especially in the overlying green marlstone 616.605 to 616.545 mbsf;
238 Figure 3, Pl.1,2). The lowermost transitional unit contains several distinct layers of pyrite
239 (Figure 3; Pl. 6), while the green marlstone contains a diffuse pyritic interval between 616.56
240 and 616.545 mbsf (Figure 3, Pl. 1,2)¹³ with two thin concentrated layers, as well as several
241 large (cm-sized) pyrite nodules⁴³. A distinct band of pyrite also occurs at 617.24 to 617.25
242 mbsf. Two other intervals contain abundant pyrite without a corresponding peak in charcoal,
243 a band at 617.0 to 616.99 mbsf (Figure 3, Pl. 5) at the base of the interval of soft sediment
244 deformation, and two lenses at 617.22 to 617.24 mbsf.

245

246 Charcoal is high-grade and preserves original wood structure (Supplemental Materials Figure
247 3; Pl. 1-12); petrified wood composed of C, P, and Si as analyzed in Energy Dispersive X-ray
248 Spectrometry (EDS) is also found (Figures 4, Pl. 10-12; Supplemental Figure 4; Pl. 10-12).
249 Pyrite in all intervals is preserved as 5-100 μm rhombic and hexagonal sheet-like crystals
250 (Supplemental Materials Figure 4; Pl. 1), and as 10-75 μm long blades that look like shards at
251 the base of the green marlstone (Figure 4; Pl. 1, 2; Supplemental Materials Figure 4; Pl. 5;
252 Supplemental Materials Figure 5; Pl. 7-9). BSE images of hexagonal and blade-like pyrite
253 often show remnant woody structure including grainy texture and pits, even in the intervals
254 where charcoal is rare or absent (Figure 4, Pl. 4-6); images also illustrate grains that preserve
255 a transition between partially- and more fully-pyritized areas (Figure 4; Pl. 4, 5). BSE images

256 of pyrite grains from the base of the transitional unit show delicate needle clusters that we
257 interpret as pyritized conifer needles (Figure 4; Pl. 7, 8; Supplemental Materials Figure 4; Pl.
258 4). The organic matter of these needles is exposed when damaged by the electron beam
259 (Supplemental Materials Figure 4; Pl. 7-9). Both upper and lower transitions contain up to 400
260 μm unburned woody material, sometimes with delicate organic structures (Supplemental
261 Materials Figure 3, Pl. 10,11).

262

263 2.3 He isotopes

264 We have measured ^3He on two samples from the uppermost transitional unit and combine
265 these data with values from Lowery et al. (2018⁴¹). Compared to deeper in the transitional unit,
266 measurements at 616.605 and 616.57 mbsf show increasing ^3He contents which suggest slower
267 sedimentation rates (Figure 2; see Supplemental Materials Table 2).

268

269 2.4 Stable O and C isotopes

270 Bulk carbonate $\delta^{18}\text{O}$ values lie between -6.5 and -8.7 ‰ in the uppermost suevite and
271 lowermost transitional unit (617.42 to 617.31 mbsf), then increase to -6.8 to -5.7 ‰ for most
272 of the transitional unit (617.24 to 616.73 mbsf), then show a steady increase to -2.3 ‰ just
273 above the green marlstone (616.54 mbsf) (Figure 5). Bulk carbonate $\delta^{13}\text{C}$ values generally
274 increase through the uppermost suevite and transitional unit (617.47 to 616.73 mbsf) from 0.48
275 ‰ to 1.45 ‰, although an interval of low values also occurs in the interval of soft-sediment
276 deformation, including samples at 616.93 to 616.84 mbsf (Figure 5). Values decrease at the
277 top of the transitional unit and within the lower green marlstone (between 616.73 and 616.57

278 mbsf) from 1.45 to 0.75 ‰ then increase through the remainder of the green marlstone and the
279 white limestone from 0.75 (616.5 mbsf) to 1.44 ‰ (616.25 mbsf).

280

281 2.5 Clumped isotopes

282 Clumped isotope-based temperatures are 88 ± 11 °C (1σ) for the uppermost suevite (617.47 to
283 617.34 mbsf), 73 ± 13 °C (1σ) for most of the transitional unit (617.31 to 616.64 mbsf) (Figure
284 5), and decrease within the uppermost transitional unit and green marlstone to 27 ± 7 °C in the
285 overlying Danian foraminiferal limestone (616.54 to 616.25 mbsf).

286

287 2.6 Strontium isotopes and trace elements

288 Strontium isotopic compositions ($^{87}\text{Sr}/^{86}\text{Sr}$) of sample aliquots leached in 0.1 M ammonium
289 acetate-acetic acid buffer (pH 4.7) and 0.1 N HCl are similar suggesting that Sr is derived from
290 carbonate (see Supplemental Materials Figure 6c). There is likewise no correlation between Sr
291 and lithogenic indicators such as Al that suggests an influence of clay dissolution on $^{87}\text{Sr}/^{86}\text{Sr}$.
292 The $^{87}\text{Sr}/^{86}\text{Sr}$ ratios of weak HCl-soluble sediment systematically decrease in the lower
293 transitional unit to ~ 0.70763 in the slump, and then increase to ~ 0.70771 in the upper
294 transitional unit (Figure 5). More radiogenic values (0.70782-0.70789) are recorded in the
295 overlying green marlstone and Danian foraminiferal limestone, values that exceed
296 contemporaneous K-Pg boundary seawater ($\leq 0.707828 \pm 0.000004^{47}$).

297

298 2.7 Micropaleontology

299 Samples from the lowermost and uppermost transitional unit and the green marlstone were
300 taken every 0.5 cm for nannoplankton and 2 cm for palynomorphs. Thin sections were also

301 observed in both intervals. Nannoplankton in the lowermost transitional unit include rare
302 specimens of Upper Cretaceous species along with rare specimens of the survivors
303 *Braarudosphaera* spp., *Cyclagelosphaera reinhardtii*, and *Zeugrhabdotus sigmoides*
304 (Supplemental Materials Figure 7; Pl. 1-4, 9, 10). A single specimen of the basal Danian
305 marker, *Biantholithus sparsus* is observed at 617.295 mbsf (Supplemental Materials Figure 7;
306 Pl. 5, 6). Dinoflagellates in the lower interval (at 617.3 mbsf) are rare but exclusively
307 represented by the cyst *Trithyrodinium evittii* (Supplemental Materials Figure 7; Pl. 11, 12).
308 Nannoplankton in the green marlstone (616.58 to 616.545 mbsf) include abundant small
309 fragments of a primitive form of *Cervisiella* spp. (Supplemental Materials and Supplemental
310 Materials Figure 7; Pl. 7, 8), but lack the Cretaceous survivor taxa with only very rare reworked
311 specimens of long-ranging Cretaceous species. A single specimen of the earliest Danian genus
312 *Neobiscutum* is observed at 616.575 mbsf (Supplemental Materials Figure 8; Pl. 9). There are
313 no organic-walled dinoflagellates in the green marlstone but cyanobacterial fossils are
314 common⁴⁴ (Supplemental Materials Figure 8; Pl. 1-8). The green marlstone also contains a
315 diverse and abundant assemblage of planktic and benthic foraminifera (the latter represented
316 by at least 63 species typical of the “Velasco Fauna”⁴⁸). Earliest Danian planktic foraminifera
317 here include *Parvularugoglobigerina*, *Woodringina*, *Praemurica*, *Eoglobigerina*, and the
318 Cretaceous survivor, *Guembelitria*⁴¹.

319

320 A diverse array of microfossils composed of apatite are observed in thin section in the green
321 marlstone between 616.58-616.56 mbsf: (1) 25-100 μm pellets consisting of micron-sized
322 clusters of ellipsoidal to spherical forms, often showing concentric layers (Figure 6; Pl. 1-3;
323 Supplemental Materials Figure 9; Pl. 1-4, 7-9); similar size and shaped objects often have

324 round, ellipsoidal and disk-shaped particles (Supplemental Materials Figure 10; Pl. 10-16) ;
325 (2) Large (~600 μm) pieces of apatite with irregular, cylindrical pores often containing small
326 apatite spheres (Figure 6; Pl. 5-7; Supplemental Materials Figure 9; Pl. 18-20); (3)
327 Arrangements of thin 1-5 (μm), elongated pieces of apatite in a skeletal-like structure (Figure
328 6; Pl. 13-16; Supplemental Materials Figure 10; Pl. 4, 6-8); and (4) More common 50 to 200
329 μm , elongate, often wispy blades or lenses of apatite with a sub-horizontal orientation that are
330 commonly fractured, hooked, and rarely coiled (Figure 6; Pl. 9-12; Supplemental Materials
331 Figure 10; Pl. 1-3, 5, 6-30). Although the blades are largely recrystallized, their internal texture
332 sometimes reveals discrete striations (200-800 nm in thickness) (Figure 6, Pl. 10;
333 Supplemental Materials Figure 10; Pl. 22, 23). These objects are also rare in the lowermost
334 transitional unit. The apatite blades appear to penetrate surrounding sediment (Supplemental
335 Materials Figure 10; Pl. 16, 17) indicating overgrowth or dissolution in the compacting
336 sediment column, while carbonate grains continued to coalesce around them (Figure 6; Pl. 9).

337

338 **3. Discussion**

339

340 3.1 Origin of micrite in the transitional unit and green marlstone

341 Samples in the upper part of the suevite contain very rare Ca-rich spherules and accretionary
342 lapilli (Figure 1; Pl. 11) similar to those described in other K-Pg boundary sections⁴⁶, areas of
343 silicate melt and clay lenses that appear to be altered silicate impact melt (Figure 1; Pl. 10),
344 and elliptical areas filled with mixed fine grained silicate and CaCO_3 , likely carbonate ash-
345 filled bubbles (Figure 1; Pl. 12; Supplemental Materials Figure 1; Pl. 11, 12 Supplemental
346 Materials Figure 2; Pl. 7-12). The spherules and lapilli were part of the Chicxulub ejecta

347 transported back to the crater by the tsunami. The highly angular shape and variable size of the
348 majority of micrite in the transitional unit (Figure 1; Pl. 3-6) may be partially related to the
349 lower energy of the seiche waves, but likely indicate a different origin.

350

351 Waters in the nascent Chicxulub crater would have been Ca-rich as a result of the interaction
352 with the products of degassed target limestone and anhydrite, thus it is possible that calcite
353 could have precipitated directly from early crater waters. Calcite (and aragonite) precipitated
354 from seawater in whittings or from fluids in hot springs shows regular prismatic or trigonal
355 crystals^{49,50}, very different from the irregular texture of micrite in the transitional unit. The
356 transitional unit texture strongly resembles that of calcite derived by thermal decarbonation
357 along fault zones^{51 52} (Figure 7; Pl. 9 compare with Pl. 10) and experimentally⁵³. Moreover,
358 transmission electron microscope (TEM) images of a sample at 617.15 mbsf reveals regular
359 ~100 nm-spaced lineations that resemble features in experimental decarbonation of Iceland
360 spar⁵⁴ (Figure 7; Pl. 1-6 compare with Pl. 11, 12). These properties suggest that production of
361 the angular micrite in the transitional unit involved decomposition of carbonate particles to
362 CaO during shock devolatilization followed by entrainment in the low velocity ejecta at the final
363 stages of excavation, rather than from the hot vapor-rich cloud. Models indicate solid particles
364 will remain internal to the Chicxulub crater or be ejected just outside it in the final stages of
365 crater excavation when ejection velocities are relatively slow⁵⁵. Externally ejected material
366 would have been delivered to the peak ring site by resurge most likely via the breach in the
367 crater rim to the northeast⁵⁶. Subsequent carbonation or backreaction of CaO to CaCO₃⁴⁵ likely
368 took place in the water column during suspension and settling; however, particles appear to
369 have grown around grains such as apatite (Figure 6; Pl. 9, 13; Supplemental Materials Figure

370 10; Pl. 4, 5, 12), suggesting continued precipitation during early burial. The green marlstone
371 also contains abundant micrite (Supplemental Materials Figure 11) along with clay and
372 calcareous microfossils⁴¹. This micrite commonly shows a Moiré fringe in TEM (Figure 7; Pl.
373 8, 9) suggesting fine overlapping crystals. More diagnostically, the micrite strongly resembles
374 micrite in the transitional unit showing low-order birefringence colors under cross-polarized
375 light, likely as a result of the sheet-like nature of decarbonated calcite, and is distinct from
376 micrite in the white limestone whose high-order birefringence colors resemble diagenetic
377 calcite (Supplemental Materials Figure 11). This suggests that at least a fraction of the micrite
378 in the green marlstone was also derived via backreaction in the water column, or possibly in
379 the vapor plume (fine carbonate dust).

380

381 3.2 The stratigraphic significance of charcoal layers

382 The stratigraphic overlap of pyrite and charcoal, and the preservation of wood structures
383 (Figure 4; Pl. 1-8) suggest that the majority of pyrite replaced wood fragments transported into
384 the crater from land or charcoaled during or after the impact process^{57 58}, possibly through
385 bacterial sulfate reduction. One hypothesized origin of charcoal is ignition of vegetation
386 around the Gulf of Mexico by thermal radiation emitted by the impact plume or by wildfires
387 ignited by ejecta heating the atmosphere^{13,57,59}. The 10-cm thick crossbedded unit at the top of
388 the suevite (Figure 2) was interpreted to be deposited by the reflected rim-wave tsunami,
389 supported by the presence of soil-derived biomarker perylene in this otherwise marine
390 sequence¹¹. The position of the lower charcoal layers directly above this suggests that the
391 charcoal and wood were also transported into the crater by the rim-wave tsunami and settled
392 out more slowly than the sand fraction as energy declined¹³.

393

394 Pyritization can exaggerate the original charcoal abundance, and create artificial bedforms, as
395 in the case of the upper layers near the top of the green marlstone where the growth of large
396 pyrite crystals outline what appears to be a ripple (Figure 3; Pl. 1, 2). In fact, finely dispersed
397 pyrite is more or less evenly distributed along the layers. Although it is hard to rule out wood
398 and charcoal derived from land, blades of pyrite (Figure 4; Pl. 1, 2; Supplemental Materials
399 Figure 4; Pl. 5; Supplemental Materials Figure 5; Pl. 7-9) in the thin uppermost (616.55 to
400 616.56 mbsf) layers (Figure 2) may be altered charcoal shards delivered by airfall, a hypothesis
401 proposed by Gulick et al. (2019)¹³ given that tsunami deposits would not be expected years
402 after impact. This interpretation is supported by the overlap of the upper layers with the Ir
403 anomaly which represents the atmospheric fallout of fine extraterrestrial material⁴³, as does
404 clay in the marlstone.

405

406 3.3 Duration of the transitional unit and green marlstone

407 Both chemical leaches show a significant decrease in micrite $^{87}\text{Sr}/^{86}\text{Sr}$ in the lower part of the
408 transitional unit, with values significantly lower than the $^{87}\text{Sr}/^{86}\text{Sr}$ of contemporaneous global
409 seawater at 66 Ma^{60,61} (~0.707824 – 0.707832; Figure 5; Supplemental Materials Figure 6c).
410 Hypotheses explaining the micrite $^{87}\text{Sr}/^{86}\text{Sr}$ values include vaporization of the impactor or
411 target limestone⁶². If micrite chemistry does indeed represent the local water column, as
412 hypothesized above, then this suggests the impactor delivered enough Sr to the water column
413 to alter its $^{87}\text{Sr}/^{86}\text{Sr}$, though this is likely limited to the local basin⁶⁰. Assuming that (i) this shift
414 was instantaneous, (ii) the impactor had an $^{87}\text{Sr}/^{86}\text{Sr}$ of ~0.703⁶³, and (iii) seawater Sr
415 concentration is the same as modern (~90 μM), the impactor delivered ~6 · 10⁵ mol of Sr to the

416 local basin (this estimate would be higher if we accounted for active exchange with seawater
417 and/or radiogenic hydrothermal inputs). If we assume an impactor volume of 525 km^3 , and a
418 density of 2 to 3 g/cm^3 , appropriate for carbonaceous chondrite, we estimate an impactor mass
419 of 1 to $1.6 \cdot 10^{15} \text{ kg}^{64}$. If the impactor had bulk Sr concentrations of ~ 5 to 15 ppm^{65-67} , then we
420 would estimate that only a very small fraction ($<0.001\%$) of the impactor would have had to
421 solubilize. Alternatively, assuming ~ 200 to 600 ppm Sr in the target rocks^{68,69}, we estimate
422 that $>4 \cdot 10^9 \text{ kg}$ of solubilized rock could explain micrite $^{87}\text{Sr}/^{86}\text{Sr}$; this estimate depends heavily
423 on the assumption of the target rock $^{87}\text{Sr}/^{86}\text{Sr}$, which could reasonably vary between ~ 0.70755
424 and 0.70765 (the latter of which is identical to the minimum micrite $^{87}\text{Sr}/^{86}\text{Sr}^{62}$). Regardless of
425 source, $^{87}\text{Sr}/^{86}\text{Sr}$ of the transitional unit suggests an age close to that of the impact, consistent
426 with ^3He isotope-based and biostratigraphic age controls⁴¹.

427

428 The ^3He technique assumes constant accumulation of cosmic-dust-derived ^3He in sediments
429 and provide detailed interpretations of accumulation rate⁷⁰. ^3He isotope data indicate extremely
430 rapid deposition for the majority of the transitional unit⁴¹, and, new measurements
431 (Supplemental Materials) suggest a significant slowdown in rates in the uppermost few cm
432 (Figure 2). Although the likely duration of the transitional unit is below the resolution for the
433 technique, ^3He isotope data are consistent with the lower part of the transitional unit
434 representing months, and the entire unit representing an interval no more than years, a duration
435 that is consistent with the presence of the Ir anomaly beginning 2 cm from the top of the unit,
436 indicating deposition within, at most, a few years. The slow-down in sedimentation rates
437 continues in the green marlstone as the driver of deposition switched from waning impact
438 energy and atmospheric fallout to hemipelagic sedimentation.

439

440 The age of the condensed green marlstone is more problematic as estimates derived from
441 impact-derived materials are in apparent conflict with those from traditional biostratigraphy
442 and ^3He isotope data. Impact-related materials include the peak of the Ir anomaly between
443 616.55 and 616.60 mbsf, the upper charcoal layers between 616.55 and 616.56 mbsf, very
444 small (40-100 μm), altered, vesicular melt particles (Supplemental Figure 2; Pl. 1-5), and, as
445 discussed, possibly fine calcite dust, immediately below the upper charcoal layers¹³. The Ir
446 anomaly generally signifies fallout with years of the impact⁷¹. These materials occur in a
447 condensed 5 cm interval which contains the first occurrence, and high abundance, of
448 *Parvularugoglobigerina eugubina* (whose appearance defines the boundary between Zones P0
449 and P α) and other common incoming Paleocene planktic foraminifera. Estimates of the base
450 of P α range from ~30 kyr to as little as 3 kyr⁷² above the K-Pg boundary with considerable
451 uncertainty (see Smit and Romein, 1985⁷³), a range that is consistent with ^3He isotope data.

452

453 The green marlstone is bioturbated⁴¹ and concentration of charcoal and wood in layers as
454 well as the foraminiferal lags (Figure 3; Pl 1) may be a result of minor winnowing, mixing
455 materials from airfall, terrestrial and pelagic sources. Ichnofacies indicates only a few cm
456 of mixing at most⁷⁴. Moreover, the apparent age dichotomy may be explained by upward
457 remobilization of Ir and other platinum group elements in reducing pore waters⁷⁵.
458 However, the distribution of impact-related materials in the green marlstone, especially the
459 lightest charcoal and woody material near the top, is also consistent with settling through
460 the water column shortly after the impact. Particles in the green marlstone have a variety
461 of sizes and would experience a range of settling rates^{76,77}. Finer material including clay⁴¹,

462 abundant 1-2 μm -sized micrite (Supplemental Materials Figure 11, Pl. 4-6), and clay-sized
463 pieces of charcoal and wood (Figure 4; Pl. 7, 8) would take several years to settle to the
464 seafloor at 600 m water depth at 25°C and normal salinity. Large ($>100 \mu\text{m}$) pieces of
465 charcoal and wood (e.g., Supplemental Materials Figure 3; Pl. 1, 3) would take a few days
466 to settle. Occurrence of larger charcoal particles near the top of the marlstone may have
467 been a result of delivery to the seafloor via density currents following gradual settling of
468 the underlying fines. Thus we conservatively interpret the marlstone to represent years to,
469 at most, millennia. We therefore interpret the appearance of the earliest Paleocene planktic
470 foraminifera in the crater in the immediate impact aftermath as part of a globally
471 asynchronous recovery with ecological implications that are explored in a later section.

472

473 3.4 Evidence for hydrothermal circulation in the early crater

474 Heat and impact-induced rock fracturing and subsequent input of water at Chicxulub are
475 thought to have generated a hydrothermal system, driven by the elevated temperatures of the
476 melt sheet and uplifted lower crustal rocks in the crater center, that models suggest lasted for
477 over 1.5-2.5 Myr²². Indeed, evidence for hydrothermal alteration is observed in granites and
478 suevites at Site M0077^{26,39}. Here we constrain the intensity of the hydrothermal system at the
479 seafloor, and its impact on the crater environment, by determining temperatures and fluid
480 chemistry during the deposition of the transitional unit and green marlstone using clumped,
481 strontium and stable carbon and oxygen isotopes.

482

483 The isotopic composition of micrite would have been first imprinted at the time and site of
484 carbonation, followed possibly by subsequent change during recrystallization to more stable

485 forms in the sediment column. Traditional oxygen isotope temperatures measured on calcium
486 carbonate ($\delta^{18}\text{O}_{\text{CaCO}_3}$) are limited by uncertainty in the isotopic composition of the water in
487 which precipitation took place. Assuming a seawater $\delta^{18}\text{O}$ value of -1.0‰ , the traditional
488 oxygen isotope thermometer indicates largely invariant temperatures of $41 \pm 4\text{ °C}$ (\pm values
489 are 1 standard deviation of the pooled analyses) within the transitional unit, with higher
490 temperatures in the underlying uppermost suevite ($54 \pm 2\text{ °C}$), and a return to normal ocean
491 temperatures in the overlying pelagic limestone ($22 \pm 2\text{ °C}$) (Figure 5). The clumped isotope
492 paleothermometer, however, is independent of assumptions about the isotopic composition of
493 the water^{78 79} and thus is advantageous for determining the temperature of the early crater.
494 Very rapid precipitation could result in meta-stable carbonates susceptible to recrystallization
495 during early burial and, if so, the clumped isotope temperatures would reflect, at least in part,
496 temperatures prevailing during recrystallization in the sediment column⁸⁰. Clumped isotope-
497 based temperatures are $73 \pm 13\text{ °C}$ (1σ) with no clear trends for most of the transitional unit
498 (Figure 5) and decrease within the green marlstone to $27 \pm 7\text{ °C}$ in the overlying Danian
499 foraminiferal limestone.

500

501 Together with $\delta^{18}\text{O}_{\text{CaCO}_3}$ values, the clumped isotope temperatures permit calculation of the
502 apparent isotopic composition of water ($\delta^{18}\text{O}_w$) in which carbonates formed. For the
503 transitional unit, this approach yields a mean $\delta^{18}\text{O}_w$ value of $+4.3 \pm 1.9\text{‰}$ (Figure 8). This
504 value is $\sim 3\text{‰}$ higher than any plausible open-ocean surface $\delta^{18}\text{O}$ value for the latest
505 Cretaceous. We offer two endmember scenarios that could result in such high apparent $\delta^{18}\text{O}_w$
506 values. In the first scenario (Figure 8A), the high values represent actual water isotopic
507 compositions, with the water being enriched in ^{18}O due to extensive evaporation of seawater

508 from heat generated by the impact event, or via high-temperature exchange with rock-derived
509 O (which is enriched in ^{18}O relative to seawater) from the water circulating through the impact
510 melt rocks and suevite (or a combination of both). In this scenario, the $\sim 70\text{ }^\circ\text{C}$ clumped isotope
511 temperatures of the transitional unit reflect actual water temperatures during initial carbonate
512 mineralization in the water column or during early burial. This scenario is possibly supported
513 by the occurrence of evaporite minerals in the upper and lower transitions (Figure 9; Pl. 1-9;
514 Supplemental Materials Figure 12; Pl. 1-3; see Supplemental Materials). These minerals could
515 be precipitates from local evaporation of seawater at the time of impact or trace residual of the
516 target rocks.

517

518 In a second scenario (Figure 8B), the carbonates initially formed in seawater of ‘normal’ $\delta^{18}\text{O}$
519 ($\sim -1\text{‰}$) at temperatures indicated by the oxygen isotope thermometry (generally in excess of
520 $30\text{ }^\circ\text{C}$ but cooler than $60\text{ }^\circ\text{C}$). During early burial on the warmer seafloor, the carbonates
521 recrystallized under rock-buffered conditions (low water/rock ratio with respect to oxygen
522 atoms) such that the clumped isotope temperatures recorded by carbonates increased, but the
523 $\delta^{18}\text{O}_{\text{CaCO}_3}$ value remained largely the same. This pattern is commonly seen in clumped isotope
524 studies of diagenetically-altered carbonate sediments⁸¹⁻⁸³, and results in fictive $\delta^{18}\text{O}_w$ values
525 that are higher than plausible seawater values. Under this scenario, the actual seafloor
526 temperatures were at least as high as the temperatures recorded by clumped isotopes (73 ± 13
527 $^\circ\text{C}$); if the carbonates were not completely recrystallized at this time (*i.e.*, if they retained some
528 of the isotopic signature attained prior to burial), then seafloor temperatures must have been
529 even higher. We disfavor this in situ high-temperature alteration scenario for three reasons.
530 First, as discussed in more detail below, heat flow models suggest that the $>130\text{m}$ -thick mantle

531 of tsunami and suevite deposits overlying the impact melt rock on top of the peak ring and
532 even thicker deposits overlying the impact melt sheet in the central basin would have
533 functioned as a highly-effective thermal insulator, resulting in temperatures similar to
534 overlying seawater temperatures. Seawater temperatures, in turn, would largely reflect
535 'normal' Gulf water temperatures because the volume of distal Gulf water rushing back to the
536 impact site following the impact event would have been vastly larger than the volume of
537 (initially very hot) water in the immediate vicinity of the impact. Additionally, the presence of
538 clear indicators of pelagic and benthic life in the upper part of the transitional unit suggests
539 that water temperatures at the time these sediments were deposited were not too extreme for
540 life. Finally, and critically, the clear decrease in C-isotope values in the interval of soft
541 sediment deformation demonstrates that C isotope values were acquired prior to burial, i.e.
542 represent water column values (Figure 5) and this interpretation is supported by the lack of
543 textural difference in micrite in this interval (Supplemental Materials Figure 1; Pl. 3).

544

545 We also disfavor interpretations invoking kinetic fractionation as the primary explanation of
546 the stable isotope data. The clumped isotope data do not record the extremely high-temperature
547 processes within the initial vapor plume that would have prevailed during decarbonation and
548 possibly during recarbonation in the plume. Mass independent triple oxygen isotope
549 fractionation ($^{17}\text{O}/^{16}\text{O}$ relative to $^{18}\text{O}/^{16}\text{O}$) during decarbonation has been shown
550 experimentally⁸⁴, with CO_2 anomalously-enriched in ^{17}O and CaO anomalously depleted, with
551 differences in $\Delta^{17}\text{O}$ of ~400 per mg between the two phases. High-precision triple oxygen
552 isotope measurements of a sample from the transitional unit and a sample from the overlying
553 Danian foraminiferal limestone show no significant deviation from compositions expected for

554 equilibrium with seawater (Supplementary Materials Figure 12 and Supplementary Materials),
555 indicating that the carbonates do not contain O inherited from the precursor CaO or CO₂
556 generated in the impact plume, unless the recombination was fortuitously stoichiometric, such
557 that the negative and positive $\Delta^{17}\text{O}$ anomalies precisely canceled. Carbon isotope compositions
558 show no evidence of kinetic fractionation and are within the range expected for latest
559 Maastrichtian and earliest Danian carbonates. Finally, timescales for oxygen exchange
560 between DIC and water are extremely rapid at elevated temperatures; for example, at 50 °C,
561 $t_{1/2} = 420$ s for HCO₃⁻-dominated solutions, and $t_{1/2} = 11.5$ h for CO₃²⁻-dominated solutions,
562 based on kinetic data from Beck et al. (2005)⁸⁵. Therefore, carbonate formation would need to
563 be extremely rapid in order to incorporate DIC in isotopic disequilibrium with seawater. If the
564 carbonate growth were this rapid, the resulting carbonates would likely be metastable (poorly-
565 ordered, high surface area) and hence susceptible to isotope exchange during recrystallization.
566 Collectively, these lines of evidence argue against a strong kinetic fractionation signal
567 preserved in isotopic compositions of the transitional unit carbonates.

568

569 The initial resurge flooded the > 1 km deep impact basin, covering the peak ring with ~ 600-
570 meters of relatively cool Gulf of Mexico waters⁴¹. The 130 meter-thick suevite section at Site
571 M0077 would have thermally isolated the deep waters from the underlying granitoid rocks and
572 impact melt during the deposition of the transitional unit as conduction would have been too
573 slow to warm even the bottom of the ocean. The central melt sheet, which is over 10 km from
574 the peak-ring site and covered by several hundred meters of suevite²², also cannot have
575 maintained warmer water temperatures within the entire impact basin during the formation of
576 the transitional unit. Thus we postulate that the carbonation took place nearer to the central

577 melt sheet where deep waters would have been heated by interactions with melt as well as via
578 ejection of hot fluids at hydrothermal vents. Precipitation of carbonate in such an
579 environment would have been promoted not only by the returning CaO flux, but also by the
580 decreased solubility of carbonate in the high-temperature waters⁸⁶⁻⁸⁸ and by increased rates
581 of backreaction in such waters⁸⁹. Thus regardless of origin, seawater in proximity of the central
582 melt sheet may have precipitated voluminous micrite, a literal carbonate “factory” (Figure
583 10A). Yet CaO ejecta and subsequent backreaction would have been crater-wide and likely
584 greater, as resurge and later seiches transported these ejecta back into the crater. Thus it is
585 likely that transitional unit micrite was derived from a wide region but with a larger proportion
586 from waters near the central melt sheet. We thus view the clumped isotope values in the
587 transitional unit as representing some of the warmest, but possibly not the highest temperatures
588 in the nascent crater.

589

590 Hydrothermal venting near the central melt sheet would have been widespread and intensive
591 ²². Such venting would leave an imprint on the trace element chemistry of the waters in which
592 the transitional unit micrite formed. The abrupt increase in ⁸⁷Sr/⁸⁶Sr above 616.65 mbsf (Figure
593 5) occurred over intervals of years to, at most, millennia, as argued above. This is more rapid
594 than rates of evolution of seawater ⁸⁷Sr/⁸⁶Sr which are much slower as reflected by the
595 residence time (5 million years) and cannot be a consequence of mass delivered by the
596 impactor. Assuming an estimated mass of water of $\sim 1.6 \cdot 10^{11}$ kg (180 km diameter, 1 km
597 average depth) in the local basin, a ~ 100 year time frame and a moderate amount of exchange
598 with seawater (i.e., the water residence time in the crater is ~ 0.05 to 1 yr) suggests a Sr mass
599 flux of $\sim 10^6$ to $2 \cdot 10^7$ mol Sr/yr and a crater water column Sr concentration that increases by

600 7%. The rate of change at Site M0077 must therefore reflect local input of radiogenic Sr,
601 possibly from hydrothermal alteration of underlying crust, consistent with clumped isotope
602 temperatures. The impact melt sheet is thought to have an average (granitic) crustal
603 composition⁹⁰, suggesting that the micrite $^{87}\text{Sr}/^{86}\text{Sr}$ reflects a water column that is influenced
604 by the hydrothermal alteration of granitic composition rocks near the central melt sheet.
605 Significantly from a stratigraphic viewpoint, the ordered progression of Sr isotope ratios
606 indicates a gradually evolving crater chemical system as well as a batch-like supply of micrite
607 to the peak ring site.

608

609 The acetic-soluble $^{87}\text{Sr}/^{86}\text{Sr}$ trend is broadly comparable to those of Fe/Ca and Mn/Ca,
610 (Supplemental Materials Figure 6b) and both trace elements are enriched throughout most of
611 the transitional unit, consistent perhaps with higher temperatures. In addition, Mg/Ca values
612 are ~11 to 14 mmol/mol in the transitional unit (and only ~20 mmol/mol in the HCl-soluble
613 fraction), which are considerably higher than biogenic carbonates. Assuming recent
614 constraints on the equilibrium partitioning behavior of Mg into calcite⁹¹ are appropriate, and
615 that the measured Mg/Ca reflects inorganic CaCO_3 precipitation, pore fluid Mg/Ca would have
616 to be extremely low (<0.1) to explain these values. Such a low value is consistent with
617 hydrothermal input that is Mg-poor, such as might be expected in a granite-hosted system.

618

619 The transitional unit also contains the following mineralogical evidence of in situ
620 hydrothermal alteration: (1) Isolated grains of ZnS are observed in the upper pyrite layers
621 at the base of the green marlstone (616.56 to 616.55 mbsf) and in a thin chlorite vein in the
622 transitional unit at 616.96 to 616.91 mbsf (Figure 9; Pl. 10, 11; Supplemental Materials

623 Figure 5; Pl. 11, 12; Supplemental Materials Figure 12; Pl. 4-6), at 617.28 to 617.26 mbsf,
624 at 617.34 to 617.32 mbsf, and at 617.54 to 617.49 mbsf. (2) At the basal contact of the
625 transitional unit 617.33 to 617.3 mbsf), pyrite appears to occur in veins filled with chlorite
626 and minor calcite that resemble fluid escape structures³⁹ (Figure 3; Pl. 7; Figure 9; Pl. 12;
627 Supplemental Materials Figure 12; Pl. 7-11). The occurrence of these sulfides in veins
628 suggests that they precipitated directly from hydrothermal fluids, clearly a distinct origin
629 from the sub-horizontal charcoal-derived pyrite layers. This is consistent with sulfur
630 isotope data which suggests high and low temperature generation of pyrite⁴³. The
631 occurrence of chlorite suggests pore water temperatures in excess of 300 °C, which is
632 consistent with independent temperature estimates²⁶. (3) Wood petrified by
633 phosphatization and silicification also indicates alteration by fluids, although this process
634 can occur at low temperature⁹². (4) Small grains of apatite are also observed within chlorite
635 veins (Figure 9; Pl. 7). Apatite is a common phase in pegmatites as P and Ca are
636 concentrated in late-stage magmatic fluids. Thus we suggest that these apatite grains also
637 precipitated from hydrothermal fluids.

638

639 The occurrence of pyrite in chlorite veins and ZnS within the transitional unit and at the
640 base of the overlying green marlstone indicate thin fingers of higher temperature fluids
641 penetrated the buried sediment column and that local hydrothermal activity persisted
642 possibly a for long time after normal hemipelagic deposition resumed consistent with
643 models showing a long-lived hydrothermal system at Chicxulub²². Clumped isotopes place
644 constraints on the integrated temporal duration of this hydrothermal fluid flow, because
645 internal clumping in carbonate minerals is susceptible to resetting via solid-state diffusion

646 at elevated temperatures. For sustained heating at 300 °C, kinetic models predict that
647 clumped isotopes will inherit the 300 °C signature in 10¹ to 10⁷ years (Brenner et al.
648 (2018)⁹³, Table 5). At 275 °C, approximately 10² to 10⁸ years would be required for
649 inheritance of the 300 °C signature. The fact that clumped isotopes record far cooler
650 temperatures (88 ± 11 °C and lower) indicates that the duration of transitional unit
651 hydrothermal activity was brief, a few years or less, or that fluid temperatures were cooler
652 than suggested by the presence of chlorite, or both.

653

654 Clumped isotope temperatures abruptly decline near the top of the transitional unit between
655 616.635 and 616.605 mbsf to assumed sea surface temperatures of 27 ± 7 °C within the green
656 marlstone (Figure 5). This change is coincident with the switch from material transported from
657 warmer regions of the crater to hemipelagic deposition (Figure 10B) yielding temperatures
658 that can be interpreted as in situ surface water values from plankton and backreacted calcite.
659 In fact, we postulate that surface temperatures at the peak ring site remained within a few
660 degrees of this level during the deposition of the transitional unit, and that this location was
661 representative of surface water conditions for much of the crater given its limited size. In the
662 following we explore how the unique crater environment, involving hydrothermal activity,
663 allowed life to recover and flourish in the immediate post-impact environment.

664

665 3.5 New evidence for life in the nascent crater

666 Globally, data and models suggest that the first decades after the impact were characterized by
667 low light and impact winter^{10,11 17 6,14,18}. However, our results indicate that waters in the crater
668 remained warm in the immediate post-impact interval, possibly as a result of hydrothermal

669 activity, even with the possibility of low light levels as indicated by evidence for atmospheric
670 fallout. Here we compare this environmental record with evidence for return of life to the
671 crater⁴¹.

672

673 Site M0077 contains a remarkable fossil record that illustrates rapid colonization of the newly
674 -formed crater by organisms representing a range of trophic levels (Figure 11). Survivor
675 species of nanofossils and planktic foraminifera are generally rare throughout the transitional
676 unit (as might be expected with such rapid depositional rates), although they increase in
677 relative abundance upsection⁴¹. Planktic foraminifera and nanofossil assemblages include
678 significantly older (late Campanian-early Maastrichtian) species, particularly near the base of
679 the transitional unit, indicating that at least part of the assemblage is reworked from older beds.
680 Lowery et al. (2018)⁴¹ interpreted the gradual increase in the abundance of planktic
681 foraminiferal and calcareous nannoplankton survivors at the top of the transitional unit as
682 evidence for the return of life to crater surface waters, and the presence of burrowing organisms
683 as an indication of a habitable sea bed. Here we focus on samples from the lowermost
684 transitional unit (617.24 to 617.3 mbsf) and the uppermost transitional unit and the green
685 marlstone (616.6 to 616.545 mbsf). These intervals represent lower-energy conditions as
686 tsunami and seiches waned (lowermost transitional unit) and suspended material settled out
687 and potentially less redeposition combined with a larger in situ component (uppermost
688 transitional unit and green marlstone). Both intervals might contain minor hiatuses, but there
689 is no evidence for a significant gap in deposition.

690

691 The lowermost transitional unit contains survivor nannoplankton *Braarudosphaera* spp.,
692 *Cyclagelosphaera reinhardtii*, and *Zeugrhabdotus sigmoides* (Figure 11; Supplemental
693 Materials Figure 7), taxa that are generally rare in uppermost Maastrichtian samples but
694 become common to abundant immediately above the boundary. Specimens are rare but far
695 exceed typical Late Cretaceous sample abundance; thus their occurrence is interpreted as
696 significant. The occurrence of *Biantholithus sparsus* is surprising and also significant. This
697 species which is commonly used as a marker for the K-Pg boundary has been observed below
698 the boundary only at one site likely as a result of bioturbation⁹⁴. The dinoflagellate cyst
699 *Trithyrodinium evittii* also originates and is very rare in the latest Maastrichtian^{95 94}, but
700 becomes a disaster taxon in the earliest Danian where it is highly abundant⁹⁵. Nannoplankton
701 assemblages in the green marlstone are very different, dominated by a primitive form of
702 *Cervisiella* spp. (commonly known as *Thoracosphaera*; Supplemental Materials Figure 7; Pl.
703 7, 8), which is a cyst of a calcareous dinoflagellate⁹⁶ and this taxon continues to dominate
704 samples in the overlying white limestone⁹⁷. There are no organic-walled dinoflagellates in the
705 green marlstone but calcite and apatite interpreted as fossils of cyanobacteria are common
706 (Supplemental Materials Figure 8; Pl. 1-8), an interpretation supported by organic
707 biomarkers⁹⁸.

708

709 Nannoplankton and palynomorphs are highly susceptible to reworking, especially by high-
710 energy transport processes such as tsunami and seiches. Although the lowermost transitional
711 unit contains common reworked Cretaceous species, the abundance of typical early Danian
712 taxa including the survivors *Biantholithus sparsus* and the dinoflagellate *T. evittii* suggests that
713 at least part of the assemblage represents early recovery either in waters outside the crater and

714 subsequently transported in by tsunami or possibly within the crater as tsunami energy
715 subsided (Figure 11). Species in this interval are dominated by haptophytes that grew in the
716 photic zone, indicating sunlit surface oceans, and the dinocyst *T. evittii* is considered to be
717 heterotrophic⁹⁹, which indicates food supply from primary producers, possibly nannoplankton
718 or cyanobacteria. The primary nannoplankton and dinoflagellate species in the lowermost
719 transitional unit are an unexpected discovery: direct survivors that thrived in or around the
720 nascent crater even as tsunami energy waned.

721

722 By contrast, the abundance and unusual form of *Cervisiella* in the green marlstone, coinciding
723 with the lowest occurrence of a number of incoming planktic foraminifera, including *P.*
724 *eugubina*⁴¹, is accompanied by near absence of Cretaceous taxa, suggesting that nannofossils
725 represent an in situ true recovery biota (Figure 11). Moreover, the distinct nature of nannofossil
726 assemblages from the lower and upper transitions suggests a primary environmental change
727 between these stages of the crater recovery. *Cervisiella* spp. is a dinoflagellate cyst, one of the
728 “disaster” taxa that was adapted to harsh environments and formed oceanwide blooms in the
729 extinction aftermath⁹⁷. The assemblage from the lowermost transitional unit disappeared,
730 suggesting that conditions had likely deteriorated to the point where surface oceans were
731 uninhabitable for almost all haptophyte nannoplankton and other dinoflagellates. The green
732 marlstone assemblage is unique; the lowermost samples at other proximal sites with expanded
733 records contain a mixture of *Cervisiella* spp. and other survivors¹⁰⁰, likely because they derive
734 from a higher stratigraphic level or are mixed by bioturbation or winnowing.

735

736 The environmental significance of flora and fauna in the green marlstone depends on the
737 interpretation of impact-derived materials. At face value, the co-occurrence of the Ir anomaly,
738 charcoal, and impact spherules supports the conclusion that these impact derived materials and
739 microfossils are in situ. In this case, we speculate that the nearly monogeneric *Cervisiella*
740 assemblages were a response to low light levels from dust and soot, a finding that would
741 represent a compelling link between one of the “kill mechanisms” and the plankton record. If
742 the planktic foraminifera in the green marlstone are also in situ, and not mixed relative to the
743 impact-derived materials, then it is possible that survivors and a dozen new taxa originated
744 within years of the impact which is unlikely but not impossible. Even a few thousand year-
745 long recovery, the maximum likely age for the green marlstone as discussed earlier, is far more
746 rapid than has been observed at other continental margin and open marine sites^{101,102}. Either
747 age interpretation would imply that conditions in crater waters were suitable for recovery
748 enabling a suite of planktic foraminiferal species to thrive before they were able to elsewhere.
749 How can this rapid recovery be explained?

750

751 The fossil record of the green marlstone, regardless of age interpretation, illustrates that as
752 calcareous phytoplankton were experiencing harsh surface ocean conditions in the nascent
753 crater, coexisting planktic foraminifera were recovering, even thriving⁴¹. Planktic foraminifera
754 would have required an alternative food source given the decimation of the calcareous
755 nannoplankton, their primary source in the Cretaceous. Possibilities include diatoms and
756 dinoflagellates which suffered lower extinction rates¹⁰³, although neither group is found in the
757 green marlstone. The occurrence of calcite and apatite microcrystals in the green marlstone
758 are interpreted as precipitates induced or influenced by cyanobacteria^{44,104}, and thus a

759 burgeoning microbial community may also have served as food for the recovering planktic
760 foraminiferal community and other zooplankton in the crater⁴⁴.

761

762 Perhaps the most remarkable aspect of the crater fossil record is the discovery of a diverse
763 assemblage composed of apatite, predominantly at the base of the green marlstone but with
764 a few specimens at the base of the transitional unit (Figure 6; Supplemental Materials
765 Figures 9, 10). Identification of the small fragments of fossil apatite is difficult, especially
766 since specimens appear to have been heavily overgrown, but resemblance with modern and
767 other fossil materials provides some clues. (1) The clusters of ellipsoidal and spherical
768 forms strongly resemble fossil bacteria in coprolites in size and form (Figure 6; Pl. 1-3
769 compare with Pl. 4) and the pellet structures (Supplemental Figure 9; Pl. 5, 10, 11, 13-16)
770 resemble more modern fecal pellets from a terrestrial site (Supplemental Figure 9; Pl. 6,
771 12)^{105,106 107 108-110}. (2) The large pieces of apatite are more difficult to assign because they
772 are heavily altered. The random shape and orientation of cavities differ from known
773 biogenic materials such as bone or dentin. Their size and the occurrence of small apatite
774 spheres resemble highly altered bone fragments that have been tunneled by
775 cyanobacteria¹¹¹ (Figure 6; Pl. 5-7 compare with Pl. 8; see also Supplemental Figure 9; Pl.
776 18-20)¹¹²⁻¹¹⁵. (3) The apatite blades are also heavily overgrown and most of their original
777 structure has been erased. However, obvious striations in some of these blades do appear
778 to be primary structures (Figure 6; Pl. 9, 10; Supplemental Materials Figure 10; Pl. 9, 10,
779 14, 15), and blades are often clustered (Figure 6; Pl. 11; Supplemental Materials Figure 10;
780 Pl. 1, 2). The blades, including those in clusters, are generally hooked, with claw-like
781 protrusions on the ends, resemble crustacean (e.g., copepod) appendages in size,

782 segmentation, and shape. Burial may have compressed the blades into the layered clusters.
783 Crustacean appendages are originally chitinous and have the potential to become
784 phosphatized¹¹⁶ and the underlying chitin structure can appear striated¹¹⁷, although
785 commonly occurring in spindles¹¹⁸. (4) The delicate layered structures (Figure 6; Pl. 13-
786 16; Supplemental Materials Figure 10; Pl. 4, 6-8) also resemble fossil bone, which may
787 have come from small fish living in the crater. Fossilized bone is often recognized by
788 preservation of osteocyte lacunae, although numerous fish lineages bone can also be
789 acellular¹¹⁹. As these structures are only 10-100 μm in size, they may represent juvenile or
790 small adult mesopelagic fish, rather than large predatory individuals. Selective survival and
791 rapid radiation of pelagic fishes, particularly small mesopelagic taxa is known to have
792 occurred following the K-Pg¹²⁰⁻¹²², so early recolonization by these taxa is quite possible.
793 Fish only experienced moderate levels of extinction at the K-Pg event and fish debris,
794 including teeth ¹²³, are common in both marine and continental K-Pg boundary clays,
795 including the classic Stevns Klint Fish Clay K-Pg outcrop in Denmark¹²⁴ and the recently
796 described Hell Creek section in North Dakota¹²⁵. We speculate that the coprolites, blades
797 and the piece of bone recovered from the sediments within the Chicxulub crater represent
798 the remains of pelagic metazoans, perhaps crustacean zooplankton (e.g. copepods) and
799 possibly fish that survived the extinction and were able to capitalize on the earliest Danian
800 phytoplankton food webs. The green marlstone may represent a unique preservational
801 environment where the combination of pore-water euxinia and limited burrowing activity
802 enabled the phosphogenesis of delicate specimens.
803

804 Smear slides from the lower transitional unit and the green marlstone contain clusters of
805 microglobular apatite that resemble spherulites grown in gels in the laboratory (Supplemental
806 Materials Figure 14; Pl. 1, 7-9), and microbial Paleoproterozoic phosphorite¹²⁶. A range of
807 other apatite forms are observed, which also could be of biological origin but whose affinity is
808 also unclear (Supplemental Material Figure 9; Pl. 17, 21, 22; Supplemental Material Figure
809 14; Pl. 2-6). Epifluorescence images also show the blades of apatite focused between 616.58-
810 616.56 mbsf (Figure 3; Pl. 4) as well as occurring in elongated lenses between 616.6-616.57
811 mbsf. These lenses contain rare grains of apatite (Supplemental Materials Figure 12; Pl. 12),
812 and appear to be organic-rich based on their appearance in cross-polarized light (Figure 3; Pl.
813 3). We speculate that these grains originate from microbial mats that thrived during the time
814 interval represented by the boundary between the transitional unit and the green marlstone.
815 Such mats may have occupied the shallow water regions near the crater rim and these grains
816 may have been transported by the intense storms expected with the climatic changes across the
817 K-Pg event^{127,128}.

818

819 The occurrence of microbial mats at the time of the upper transitional unit and in the green
820 marlstone has already been proposed based on elevated 3 β -methylhopane indices in samples
821 between 616.62 and 616.55 mbsf⁹⁸ which signify methanotrophic bacteria. Schaefer et al.
822 (2020)⁹⁸ postulated that the microbial compounds were redeposited from shallower parts of
823 the crater. Today phosphatized microbial mats accumulate in upwelling settings along
824 continental margins where the flux of organic carbon results in pore water supersaturation and
825 subsequent precipitation of apatite following bacterial phosphate remineralization¹²⁹.
826 Phosphate is generally rare in sediments deposited in deeper ocean regions. Elevated P levels

827 may be a response to eutrophication that followed the decimation of planktic producers at the
828 K-Pg boundary¹³⁰; indeed apatite fossils are also found in samples from the Fish Clay at Stevns
829 Klint (Supplemental Materials Figure 14; Pl. 10-12) that are thought to date to centuries and
830 millennia after the impact. Resurge into the crater via the ~2 km deep northeast ramp to the
831 Gulf of Mexico⁵⁶ (Figure 10) could have delivered nutrient-rich waters but microbial activity
832 would have readily depleted nutrient levels; thus there is likely another source of P. Occurrence
833 of apatite in chlorite veins lower in the transitional unit (Figure 9; Pl. 7) suggests a connection
834 between hydrothermal activity and P supply; indeed P is often enriched in late stage pegmatite
835 fluids¹³¹. Thus the nascent crater may have provided a productive refuge for survivors,
836 including the planktic foraminifera, explaining their earlier recovery.

837

838 Evidence for diverse life including morphological and molecular fossils^{41 44,104} (this study)
839 from Chicxulub suggests that the crater became rapidly habitable in the immediate aftermath
840 of the impact (Figure 11), possibly earlier than in other parts of the ocean. This suggests that
841 the unique crater environment allowed life to flourish. We speculate that heat and nutrients
842 from the hydrothermal system were instrumental in sustaining a diverse community of
843 primitive life, and this community likely played a role in survival of higher orders of
844 organisms, including pelagic crustaceans and fish¹²³. The rapid appearance of life in the early
845 Chicxulub crater, including organisms at a range of trophic levels, demonstrates the resiliency
846 of life under extraordinarily harsh conditions, which has important ramifications for early life
847 on Earth and life on other planets².

848

849 **4. Conclusions**

850 An expanded record from the peak ring of the Chicxulub crater illustrates the connection
851 between environment and recovery of life in the nascent Chicxulub crater. Water temperatures
852 in the were in excess of 70 °C immediately after the K-Pg impact with heat derived from the
853 central melt sheet. The cooler peak ring location was habitable within days to years of the
854 impact with survivor nannoplankton and monospecific, red-tide dinocyst assemblage arriving
855 in the aftermath of the tsunami waves. A monogeneric calcareous dinoflagellate resting cyst
856 assemblage is found at levels where charcoal and the Ir anomaly indicate atmospheric fallout,
857 and a possible interpretation is that the absence of photosynthetic plankton was a response to
858 low light levels. Microbial fossils are found throughout the sequence suggesting a thriving
859 bacterial community potentially supported by nutrients from hydrothermal activity. This
860 productivity likely supported the recovery of organisms representing a range of trophic levels
861 including planktic foraminifera, pelagic crustaceans and fishes over an interval of years to no
862 more than a few millennia.

863

864 Acknowledgments

865 This research used samples and data provided by IODP. Expedition 364 was jointly funded
866 by the European Consortium for Ocean Research Drilling (ECORD) and ICDP, with
867 contributions and logistical support from the Yucatán State Government and Universidad
868 Nacional Autónoma de México (UNAM). Research was funded by NSF-OCE OCE
869 1736951 (to TB and KHF), 1737351, 1737087, OCE 1736826, OCE 1737087, OCE
870 1737037, and OCE 1737199, and Post Expedition Awards from IODP to TB, NERC grant
871 NE/P005217/1 to JVM, and by the Swedish Research Council (VR), grant 2015-4264 to
872 VV. SG acknowledges the support by the Belgian Science Policy (BELSPO) and Research
873 Foundation - Flanders (FWO - Vlaanderen). We acknowledge helpful discussions with
874 Cristiano Colletini, Maureen Feineman, Lee Kump, Ron Shahar and Andy Smye. We thank
875 Holger Kuhlmann, Chad Broyles, and Phil Rumford for help with sampling, Julie Anderson
876 and Wes Auken for help with the SEM, Kat Crispin, Mark Fairchild and Tom Henderson
877 with help with microscopy and Jenn Grey for assistance with TEM. This is UTIG
878 Contribution #XXXX.

879

880

881 **Data Availability:** The data that support the findings of this study are available in the
882 PANGAEA database (<https://www.pangaea.de/>).

883

884

885

886 References

- 887 1 Morgan, J. *et al.* The formation of peak rings in large impact craters. *Science* **354**,
888 878-882 (2016).
- 889 2 Russell, M. J. & Hall, A. J. The onset and early evolution of life. *Memoirs-*
890 *Geological Society of America* **198**, 1 (2006).
- 891 3 Hildebrand, A. R. *et al.* Chicxulub crater: a possible Cretaceous/Tertiary
892 boundary impact crater on the Yucatan Peninsula, Mexico. *Geology* **19**, 867-871
893 (1991).
- 894 4 Kring, D. A. & Boynton, W. V. Petrogenesis of an augite-bearing melt rock in the
895 Chicxulub structure and its relationship to K/T impact spherules in Haiti. *Nature*
896 **358**, 141 (1992).
- 897 5 Schulte, P. *et al.* The Chicxulub asteroid impact and mass extinction at the
898 Cretaceous-Paleogene boundary. *Science* **327**, 1214-1218,
899 doi:10.1126/science.1177265 (2010).
- 900 6 Vellekoop, J. *et al.* Rapid short-term cooling following the Chicxulub impact at
901 the Cretaceous–Paleogene boundary. *Proc Natl Acad Sci U S A* **111**, 7537-7541
902 (2014).
- 903 7 Prinn, R. G. & Fegley Jr, B. Bolide impacts, acid rain, and biospheric traumas at
904 the Cretaceous-Tertiary boundary. *Earth and Planetary Science Letters* **83**, 1-15
905 (1987).
- 906 8 Alvarez, L. W., Alvarez, W., Asaro, F. & Michel, H. V. Extraterrestrial cause for
907 the Cretaceous-Tertiary extinction. *Science* **208**, 1095-1108 (1980).
- 908 9 Toon, O. B. *et al.* Evolution of an impact-generated dust cloud and its effects on
909 the atmosphere. (1982).
- 910 10 Brugger, J., Feulner, G. & Petri, S. Baby, it's cold outside: Climate model
911 simulations of the effects of the asteroid impact at the end of the Cretaceous.
912 *Geophysical Research Letters* **44**, 419-427 (2017).
- 913 11 Artemieva, N. & Morgan, J. Quantifying the Release of Climate-Active Gases by
914 Large Meteorite Impacts With a Case Study of Chicxulub. *Geophysical Research*
915 *Letters* **44**, 10,180-110,188, doi:10.1002/2017gl074879 (2017).
- 916 12 Kring, D. A. The Chicxulub impact event and its environmental consequences at
917 the Cretaceous–Tertiary boundary. *Palaeogeography, Palaeoclimatology,*
918 *Palaeoecology* **255**, 4-21, doi:10.1016/j.palaeo.2007.02.037 (2007).
- 919 13 Gulick, S., Bralower, T.J., Ormö, J., Hall, B., Grice, K., Schaefer, B., Lyons, S.,
920 Freeman, K., Morgan, J., Artemieva, N., Kaskes, P. de Graaff, S., Whalen, M.,
921 Goto, K., Smit, J. and others. The first day of the Cenozoic. *PNAS* **113**, 19342-
922 19351 (2019).
- 923 14 Tabor, C. R., Bardeen, C. G., Otto - Bliesner, B. L., Garcia, R. R. & Toon, O. B.
924 Causes and Climatic Consequences of the Impact Winter at the Cretaceous -
925 Paleogene Boundary. *Geophysical Research Letters* **47**, e60121 (2020).

- 926 15 Wolbach, W. S., Gilmour, I. & Anders, E. Major wildfires at the
927 Cretaceous/Tertiary boundary. *Geological Society of America Special Paper* **247**,
928 391-400 (1990).
- 929 16 Tschudy, R., Pillmore, C., Orth, C., Gilmore, J. & Knight, J. Disruption of the
930 terrestrial plant ecosystem at the Cretaceous-Tertiary boundary, Western Interior.
931 *Science* **225**, 1030-1032 (1984).
- 932 17 Kaiho, K. *et al.* Global climate change driven by soot at the K-Pg boundary as the
933 cause of the mass extinction. *Scientific Reports* **6**, 28427 (2016).
- 934 18 Lyons, S. L., Karp, A.T., Bralower, T.J., Grice, K., Schaefer, B., Gulick, S.P.S.,
935 Morgan, J., Freeman, K.H.,. Cretaceous-Paleogene boundary fire markers at
936 Chicxulub sourced from fossil hydrocarbons, PNAS, in review. . *PNAS* (in
937 review).
- 938 19 Artemieva, N. & Morgan, J. Global K - Pg layer deposited from a dust cloud.
939 *Geophysical Research Letters*, e2019GL086562 (2020).
- 940 20 Hull, P. M. *et al.* On impact and volcanism across the Cretaceous-Paleogene
941 boundary. *Science* **367**, 266-272 (2020).
- 942 21 Cockell, C. S., Osinski, G. R. & Lee, P. The impact crater as a habitat: effects of
943 impact processing of target materials. *Astrobiology* **3**, 181-191 (2003).
- 944 22 Abramov, O. & Kring, D. A. Numerical modeling of impact - induced
945 hydrothermal activity at the Chicxulub crater. *Meteoritics Planetary Science* **42**,
946 93-112 (2007).
- 947 23 Osinski, G. R. *et al.* Impact-generated hydrothermal systems on Earth and Mars.
948 *Icarus* **224**, 347-363 (2013).
- 949 24 Newsom, H. E., Hagerty, J. J. & Thorsos, I. E. Location and sampling of aqueous
950 and hydrothermal deposits in Martian impact craters. *Astrobiology* **1**, 71-88
951 (2001).
- 952 25 Rathbun, J. A. & Squyres, S. W. Hydrothermal systems associated with Martian
953 impact craters. *Icarus* **157**, 362-372 (2002).
- 954 26 Kring, D. A., Tikoo, S.M., and others. Probing the hydrothermal system of the
955 Chicxulub Crater *Science Advances* (2020).
- 956 27 Cockell, C. S. C., M.J.L., Grice, K. Schaefer, B. Schnieders, L., Morgan, J.V.,
957 Sean P. S. Gulick, S.P.S., Wittmann, A. Lofi, J., Christeson, G., Kring, D.A.,
958 Whalen, M., Bralower, T.J., and others. Shaping of the present-day deep
959 biosphere by the impact catastrophe that ended the Cretaceous. *Nature*
960 *Geoscience* (in review).
- 961 28 O’Sullivan, E. M., Goodhue, R., Ames, D. E. & Kamber, B. S.
962 Chemostratigraphy of the Sudbury impact basin fill: Volatile metal loss and post-
963 impact evolution of a submarine impact basin. *Geochimica et Cosmochimica Acta*
964 **183**, 198-233 (2016).
- 965 29 Morgan, J. V. & Warner, M. Chicxulub: The third dimension of a multi-ring
966 impact basin. *Geology* **27**, 407-410 (1999).
- 967 30 Gulick, S. *et al.* Geophysical characterization of the Chicxulub impact crater.
968 *Reviews of Geophysics* **51**, 31-52 (2013).
- 969 31 Arz, J. A., Alegret, L. & Arenillas, I. Foraminiferal biostratigraphy and
970 paleoenvironmental reconstruction at the Yaxcopoil - 1 drill hole, Chicxulub

971 crater, Yucatán Peninsula. *Meteoritics & Planetary Science* **39**, 1099-1111
972 (2004).

973 32 Goto, K. *et al.* Evidence for ocean water invasion into the Chicxulub crater at the
974 Cretaceous/Tertiary boundary. *Meteoritics & Planetary Science* **39**, 1233-1247
975 (2004).

976 33 Lüders, V. & Rickers, K. Fluid inclusion evidence for impact - related
977 hydrothermal fluid and hydrocarbon migration in Cretaceous sediments of the
978 ICDP - Chicxulub drill core Yax - 1. *Meteoritics Planetary Science* **39**, 1187-
979 1197 (2004).

980 34 Zürcher, L. & Kring, D. A. Hydrothermal alteration in the core of the
981 Yaxcopoil - 1 borehole, Chicxulub impact structure, Mexico. *Meteoritics*
982 *Planetary Science* **39**, 1199-1221 (2004).

983 35 Hecht, L., Wittmann, A., R. - T., S. & Stöffler, D. Composition of impact melt
984 particles and the effects of post - impact alteration in suevitic rocks at the
985 Yaxcopoil - 1 drill core, Chicxulub crater, Mexico. *Meteoritics Planetary Science*
986 **39**, 1169-1186 (2004).

987 36 Rowe, A., Wilkinson, J., Coles, B. & Morgan, J. Chicxulub: Testing for post -
988 impact hydrothermal input into the Tertiary ocean. *Journal Planetary Science*
989 *Meteoritics* **39**, 1223-1231 (2004).

990 37 Wang, Y.-Y., Yao, Q.-Z., Zhou, G.-T. & Fu, S.-Q. Formation of elongated calcite
991 mesocrystals and implication for biomineralization. *Chemical Geology* **360**, 126-
992 133 (2013).

993 38 Whalen, M. T., Gulick, S., Pearson, Z. F. & Norris, R. D. Annealing the
994 Chicxulub impact: Paleogene Yucatán carbonate slope development in the
995 Chicxulub impact basin, Mexico. *Special Publication-SEPM* **105**, 282-304
996 (2013).

997 39 Morgan, J. & Gulick, S. Drilling the K-Pg Impact Crater: IODP-ICDP Expedition
998 364 Results. *LPI Contributions* **2067** (2018).

999 40 Gulick, S. *et al.* Expedition 364 preliminary report: Chicxulub: drilling the K-Pg
1000 impact crater. (2017).

1001 41 Lowery, C. M. *et al.* Rapid recovery of life at ground zero of the end-Cretaceous
1002 mass extinction. *Nature* **558**, 288-291, doi:10.1038/s41586-018-0163-6 (2018).

1003 42 Whalen, M., Gulick, S.P., Lowery, C.M., Bralower, T.J., Morgan, J.V., Grice, K.,
1004 Schaefer, B., Smit, J. Ormo, J., Wittmann, A., Kring, D.A., Lyons, S., Goderis, S.,
1005 Rodríguez-Tovar, F.J. and others. Winding down the Chicxulub impact: the
1006 transition between impact-related and normal marine sedimentation at ground
1007 zero. *Earth Planetary Science Letters* (In review).

1008 43 Goderis, S., H., S., Ferrière, L. & others, a. The final settling of meteoritic matter
1009 on the peak-ring of the Chicxulub impact structure at Site M0077A of IODP-
1010 ICDP expedition 364. . *Large Meteorite Impacts and Planetary Evolution VI*
1011 (2019).

1012 44 Bralower, T. J., Cosmidis, J., Heaney, P., Kump, L.R. Morgan, J., Harper, D.
1013 Lyons, S.L., Freeman, K.H., Grice, K., Wendler, J., Zachos, J.C., Artemieva, N.,
1014 Gulick, S. , House, C., Jones, H.L., Lowery, C.L., Nims, C., Schaefer, B., Si, A.,
1015 Thomas, E., Vajda, V. . Evidence for global microbial blooms during the

1016 immediate aftermath of the Cretaceous-Paleogene boundary impact. . *Earth and*
1017 *Planetary Science Letters* (in review).

1018 45 Schulte, P. *et al.* A dual-layer Chicxulub ejecta sequence with shocked carbonates
1019 from the Cretaceous–Paleogene (K–Pg) boundary, Demerara Rise, western
1020 Atlantic. *Geochimica et Cosmochimica Acta* **73**, 1180-1204,
1021 doi:10.1016/j.gca.2008.11.011 (2009).

1022 46 Yancey, T. E. & Guillemette, R. N. Carbonate accretionary lapilli in distal
1023 deposits of the Chicxulub impact event. *Geological Society of America Bulletin*
1024 **120**, 1105-1118 (2008).

1025 47 McArthur, J. & Howarth, R. (Cambridge University Press: Cambridge, UK,
1026 2004).

1027 48 Alegret, L. & Thomas, E. Upper Cretaceous and lower Paleogene benthic
1028 foraminifera from northeastern Mexico. *Micropaleontology*, 269-316 (2001).

1029 49 Jones, B. Review of aragonite and calcite crystal morphogenesis in thermal spring
1030 systems. *Sedimentary Geology* **354**, 9-23 (2017).

1031 50 Thompson, J. B. in *Microbial Sediments* 250-260 (Springer, 2000).

1032 51 Collettini, C., Viti, C., Tesei, T. & Mollo, S. Thermal decomposition along natural
1033 carbonate faults during earthquakes. *Geology* **41**, 927-930 (2013).

1034 52 Novellino, R. *et al.* Dynamic weakening along incipient low-angle normal faults
1035 in pelagic limestones (Southern Apennines, Italy). *Journal of the Geological*
1036 *Society* **172**, 283-286 (2015).

1037 53 Hamann, C. *et al.* The reaction of carbonates in contact with laser - generated,
1038 superheated silicate melts: Constraining impact metamorphism of carbonate -
1039 bearing target rocks. *Meteoritics & Planetary Science* **53**, 1644-1686 (2018).

1040 54 Rodriguez-Navarro, C., Ruiz-Agudo, E., Luque, A., Rodriguez-Navarro, A. B. &
1041 Ortega-Huertas, M. Thermal decomposition of calcite: Mechanisms of formation
1042 and textural evolution of CaO nanocrystals. *American Mineralogist* **94**, 578-593
1043 (2009).

1044 55 Kring, D. A. Hypervelocity collisions into continental crust composed of
1045 sediments and an underlying crystalline basement: Comparing the Ries (~ 24 km)
1046 and Chicxulub (~ 180 km) impact craters. *Chemie der Erde-Geochemistry* **65**, 1-
1047 46 (2005).

1048 56 Gulick, S. P. *et al.* Importance of pre-impact crustal structure for the asymmetry
1049 of the Chicxulub impact crater. *Nature Geoscience* **1**, 131-135 (2008).

1050 57 Kruge, M. A., Stankiewicz, B. A., Crelling, J. C., Montanari, A. & Bensley, D. F.
1051 Fossil charcoal in Cretaceous-Tertiary boundary strata: Evidence for catastrophic
1052 firestorm and megawave. *Geochimica et Cosmochimica Acta* **58**, 1393-1397
1053 (1994).

1054 58 Jones, T. P. & Lim, B. Extraterrestrial impacts and wildfires. *Palaeogeography,*
1055 *Palaeoclimatology, Palaeoecology* **164**, 57-66 (2000).

1056 59 Melosh, H. J., Schneider, N., Zahnle, K. J. & Latham, D. Ignition of global
1057 wildfires at the Cretaceous/Tertiary boundary. *Nature* **343**, 251 (1990).

1058 60 MacLeod, K. G., Huber, B. T. & Fullagar, P. D. Evidence for a small (~ 0.000
1059 030) but resolvable increase in seawater ⁸⁷Sr/⁸⁶Sr ratios across the Cretaceous-
1060 Tertiary boundary. *Geology* **29**, 303-306 (2001).

1061 61 Martin, E. & Macdougall, J. Seawater Sr isotopes at the Cretaceous/Tertiary
1062 boundary. *Earth and Planetary Science Letters* **104**, 166-180 (1991).

1063 62 Belza, J., Goderis, S., Keppens, E., Vanhaecke, F. & Claeys, P. An emplacement
1064 mechanism for the mega - block zone within the Chicxulub crater.(Yucatán,
1065 Mexico) based on chemostratigraphy. *Meteoritics & Planetary Science* **47**, 400-
1066 413 (2012).

1067 63 Dickin, A. P. *Radiogenic isotope geology*. (Cambridge University Press, 2018).

1068 64 Durand-Manterola, H. J. & Cordero-Tercero, G. Assessments of the energy, mass
1069 and size of the Chicxulub Impactor. *arXiv preprint arXiv:1403.6391* (2014).

1070 65 Wasserburg, G., Papanastassiou, D. & Sanz, H. Initial strontium for a chondrite
1071 and the determination of a metamorphism or formation interval. *Earth and*
1072 *Planetary Science Letters* **7**, 33-43 (1969).

1073 66 Faure, G. & Powell, J. L. in *Strontium isotope Geology* 78-91 (Springer, 1972).

1074 67 Charlier, B., Tissot, F., Dauphas, N. & Wilson, C. Nucleosynthetic, radiogenic
1075 and stable strontium isotopic variations in fine-and coarse-grained refractory
1076 inclusions from Allende. *Geochimica et Cosmochimica Acta* **265**, 413-430 (2019).

1077 68 Schmitt, R. T., Wittmann, A. & Stöffler, D. Geochemistry of drill core samples
1078 from Yaxcopoil - 1, Chicxulub impact crater, Mexico. *Meteoritics & Planetary*
1079 *Science* **39**, 979-1001 (2004).

1080 69 Tuchscherer, M. G. *The petrology and geochemistry of the impactite sequence*
1081 *and selected target rocks from the Yaxcopoil-1 borehole, Chicxulub Impact*
1082 *Structure, Yucatan Peninsula, Mexico*, (2008).

1083 70 Farley, K. & Eltgroth, S. An alternative age model for the Paleocene–Eocene
1084 thermal maximum using extraterrestrial ³He. *Earth and Planetary Science Letters*
1085 **208**, 135-148 (2003).

1086 71 Artemieva, N. & Morgan, J. Modeling the formation of the K–Pg boundary layer.
1087 *Icarus* **201**, 768-780 (2009).

1088 72 Berggren, W. A., Kent, D. V., Swisher III, C. C. & Aubry, M.-P. A revised
1089 Cenozoic geochronology and chronostratigraphy. *Geochronology, Time Scales*
1090 *and Global Stratigraphic Correlation, SEPM Special Publication No. 54* (1995).

1091 73 Smit, J. & Romein, A. A sequence of events across the Cretaceous-Tertiary
1092 boundary. *Earth and Planetary Science Letters* **74**, 155-170 (1985).

1093 74 Rodríguez-Tovar, F. J., Lowery, C., Bralower, T.J., Gulick, S., and Jones, H.
1094 Rapid macrobenthic diversification and stabilization after the end-Cretaceous
1095 mass extinction event *Nature Ecology and Evolution* (In review).

1096 75 Colodner, D. C., Boyle, E. A., Edmond, J. M. & Thomson, J. Post-depositional
1097 mobility of platinum, iridium and rhenium in marine sediments. *Nature* **358**, 402
1098 (1992).

1099 76 Stokes, G. G. On the effect of the internal friction of fluids on the motion of
1100 pendulums. *Transactions of the Cambridge Philosophical Society IX, reprinted in*
1101 *Mathematical and Physical Papers* **3**, 1–86, doi:
1102 <https://doi.org/10.1017/CBO9780511702266> (1850).

1103 77 Maggi, F. The settling velocity of mineral, biomineral, and biological particles
1104 and aggregates in water. *Journal of Geophysical Research: Oceans* **118**, 2118-
1105 2132 (2013).

- 1106 78 Ghosh, P. *et al.* 13C–18O bonds in carbonate minerals: a new kind of
1107 paleothermometer. *Geochimica et Cosmochimica Acta* **70**, 1439-1456 (2006).
- 1108 79 Eiler, J. M. Clumped-isotope geochemistry—The study of naturally-occurring,
1109 multiply-substituted isotopologues. *Earth Planetary Science Letters* **262**, 309-327
1110 (2007).
- 1111 80 Gabitov, R. I., Watson, E. B. & Sadekov, A. Oxygen isotope fractionation
1112 between calcite and fluid as a function of growth rate and temperature: An in situ
1113 study. *Chemical Geology* **306**, 92-102 (2012).
- 1114 81 Ferry, J. M., Passey, B. H., Vasconcelos, C. & Eiler, J. M. Formation of dolomite
1115 at 40–80° C in the Latemar carbonate buildup, Dolomites, Italy, from clumped
1116 isotope thermometry. *Geology* **39**, 571-574 (2011).
- 1117 82 Henkes, G. A. *et al.* Temperature limits for preservation of primary calcite
1118 clumped isotope paleotemperatures. *Geochimica et Cosmochimica Acta* **139**, 362-
1119 382 (2014).
- 1120 83 Shenton, B. J. *et al.* Clumped isotope thermometry in deeply buried sedimentary
1121 carbonates: The effects of bond reordering and recrystallization. *GSA Bulletin*
1122 **127**, 1036-1051 (2015).
- 1123 84 Miller, M. F. *et al.* Mass-independent fractionation of oxygen isotopes during
1124 thermal decomposition of carbonates. *Proceedings of the National Academy of*
1125 *Sciences* **99**, 10988-10993 (2002).
- 1126 85 Beck, W. C., Grossman, E. L. & Morse, J. W. Experimental studies of oxygen
1127 isotope fractionation in the carbonic acid system at 15, 25, and 40 C. *Geochimica*
1128 *et Cosmochimica Acta* **69**, 3493-3503 (2005).
- 1129 86 Plummer, L. N. & Busenberg, E. The solubilities of calcite, aragonite and vaterite
1130 in CO₂-H₂O solutions between 0 and 90 C, and an evaluation of the aqueous
1131 model for the system CaCO₃-CO₂-H₂O. *Geochimica et cosmochimica acta* **46**,
1132 1011-1040 (1982).
- 1133 87 Mucci, A. The solubility of calcite and aragonite in seawater at various salinities,
1134 temperatures, and one atmosphere total pressure. *American Journal of Science*
1135 **283**, 780-799 (1983).
- 1136 88 He, S. & Morse, J. W. The carbonic acid system and calcite solubility in aqueous
1137 Na-K-Ca-Mg-Cl-SO₄ solutions from 0 to 90 C. *Geochimica et Cosmochimica*
1138 *Acta* **57**, 3533-3554 (1993).
- 1139 89 Agrinier, P., Deutsch, A., Schärer, U. & Martinez, I. Fast back-reactions of shock-
1140 released CO₂ from carbonates: An experimental approach. *Geochimica et*
1141 *Cosmochimica Acta* **65**, 2615-2632 (2001).
- 1142 90 Kring, D. A. The dimensions of the Chicxulub impact crater and impact melt
1143 sheet. *Journal of Geophysical Research: Planets* **100**, 16979-16986 (1995).
- 1144 91 Lammers, L. N. & Mitnick, E. H. Magnesian calcite solid solution
1145 thermodynamics inferred from authigenic deep-sea carbonate. *Geochimica et*
1146 *Cosmochimica Acta* **248**, 343-355 (2019).
- 1147 92 Akahane, H., Furuno, T., Miyajima, H., Yoshikawa, T. & Yamamoto, S. Rapid
1148 wood silicification in hot spring water: an explanation of silicification of wood
1149 during the Earth's history. *Sedimentary Geology* **169**, 219-228 (2004).

- 1150 93 Brenner, D. C., Passey, B. H. & Stolper, D. A. Influence of water on clumped-
1151 isotope bond reordering kinetics in calcite. *Geochimica et Cosmochimica Acta*
1152 **224**, 42-63 (2018).
- 1153 94 Pospichal, J. J. & Wise Jr, S. W. Calcareous nannofossils across the K/T
1154 boundary, ODP hole 690C, Maud Rise, Weddell Sea. *Proceedings of the Ocean*
1155 *Drilling Program, Scientific Results* **113**, 515-532 (1990).
- 1156 95 Vellekoop, J. *et al.* Shelf hypoxia in response to global warming after the
1157 Cretaceous-Paleogene boundary impact. *Geology* **46**, 683-686 (2018).
- 1158 96 Brinkhuis, H., Zachariasse, W. J. & Dinoflagellate cysts, sea level changes and
1159 planktonic foraminifers across the Cretaceous-Tertiary boundary at El Haria,
1160 northwest Tunisia. *Marine Micropaleontology* **13**, 153-191 (1988).
- 1161 97 Jones, H. L., Lowery, C. M. & Bralower, T. J. Calcareous nannoplankton “boom-
1162 bust” successions in the Cretaceous-Paleogene (K-Pg) impact crater suggests
1163 ecological experimentation at “ground zero” *Geology* **47**, 753-756 (2019).
- 1164 98 Schaefer, B. *et al.* Microbial life in the nascent Chicxulub crater. *Geology*,
1165 doi:<https://doi.org/10.1130/G46799.1> (2020).
- 1166 99 Brinkhuis, H., Bujak, J., Smit, J., Versteegh, G. & Visscher, H. Dinoflagellate-
1167 based sea surface temperature reconstructions across the Cretaceous–Tertiary
1168 boundary. *Palaeogeography, Palaeoclimatology, Palaeoecology* **141**, 67-83
1169 (1998).
- 1170 100 Jiang, S., Bralower, T. J., Patzkowsky, M. E., Kump, L. R. & Schueth, J. D.
1171 Geographic controls on nannoplankton extinction across the
1172 Cretaceous/Paleogene boundary. *Nature Geoscience* **3**, 280-285,
1173 doi:10.1038/ngeo775 (2010).
- 1174 101 Birch, H. S., Coxall, H. K. & Pearson, P. N. Evolutionary ecology of Early
1175 Paleocene planktonic foraminifera: size, depth habitat and symbiosis.
1176 *Paleobiology* **38**, 374-390 (2012).
- 1177 102 Coxall, H. K., D'Hondt, S. & Zachos, J. C. Pelagic evolution and environmental
1178 recovery after the Cretaceous-Paleogene mass extinction. *Geology* **34**,
1179 doi:10.1130/g21702.1 (2006).
- 1180 103 Hull, P. M., Norris, R. D., Bralower, T. J. & Schueth, J. D. A role for chance in
1181 marine recovery from the end-Cretaceous extinction. *Nature Geoscience* **4**, 856-
1182 860, doi:10.1038/ngeo1302 (2011).
- 1183 104 Schaefer, B., Grice, K., Coolen, M.J.L., Summons, R.E., Cui, X, Bauersachs, T.,
1184 Schwark, L., Böttcher, M.E., Bralower, T.J., Lyons, S., Freeman, K.H., Cockell,
1185 C.S., Gulick, S.P.S., Morgan, J.V., Whalen, M., Lowery, C., and IODP expedition
1186 364 scientists. Microbial life in the nascent Chicxulub crater. *Geology*,
1187 doi:<https://doi.org/10.1130/G46799.1> (2020).
- 1188 105 Cosmidis, J. *et al.* Nanometer - scale characterization of exceptionally preserved
1189 bacterial fossils in Paleocene phosphorites from Ouled Abdoun (Morocco).
1190 *Geobiology* **11**, 139-153 (2013).
- 1191 106 Pesquero, M. D., Souza-Egipsy, V., Alcalá, L., Ascaso, C. & Fernández-Jalvo, Y.
1192 Calcium phosphate preservation of faecal bacterial negative moulds in hyaena
1193 coprolites. *Acta Palaeontologica Polonica* **59**, 997-1006 (2013).

- 1194 107 Cosmidis, J., Benzerara, K., Menguy, N. & Arning, E. Microscopy evidence of
1195 bacterial microfossils in phosphorite crusts of the Peruvian shelf: Implications for
1196 phosphogenesis mechanisms. *Chemical Geology* **359**, 10-22 (2013).
- 1197 108 Zatoń, M. *et al.* Coprolites of Late Triassic carnivorous vertebrates from Poland:
1198 an integrative approach. *Palaeogeography, Palaeoclimatology, Palaeoecology*
1199 **430**, 21-46 (2015).
- 1200 109 Pineda, A. *et al.* Characterizing hyena coprolites from two latrines of the Iberian
1201 Peninsula during the Early Pleistocene: Gran Dolina (Sierra de Atapuerca,
1202 Burgos) and la Mina (Barranc de la Boella, Tarragona). *Palaeogeography,*
1203 *Palaeoclimatology, Palaeoecology* **480**, 1-17 (2017).
- 1204 110 Al-Bassam, K. & Halodová, P. in *Annales Societatis Geologorum Poloniae*. 257-
1205 272, doi: 210.14241/asgp. 12018.14009.
- 1206 111 Ramírez-Reinat, E. & Garcia-Pichel, F. Prevalence of Ca²⁺-ATPase-mediated
1207 carbonate dissolution among cyanobacterial euendoliths. *Appl. Environ.*
1208 *Microbiol.* **78**, 7-13 (2012).
- 1209 112 Emslie, S. D. *et al.* Chronic mercury exposure in Late Neolithic/Chalcolithic
1210 populations in Portugal from the cultural use of cinnabar. *Scientific reports* **5**,
1211 14679 (2015).
- 1212 113 Atkins, A. *et al.* Remodeling in bone without osteocytes: billfish challenge bone
1213 structure–function paradigms. *Proceedings of the National Academy of Sciences*
1214 **111**, 16047-16052 (2014).
- 1215 114 Cohen, L. *et al.* Comparison of structural, architectural and mechanical aspects of
1216 cellular and acellular bone in two teleost fish. *Journal of Experimental Biology*
1217 **215**, 1983-1993 (2012).
- 1218 115 Seidel, R. *et al.* Ultrastructural and developmental features of the tessellated
1219 endoskeleton of elasmobranchs (sharks and rays). *Journal of anatomy* **229**, 681-
1220 702 (2016).
- 1221 116 Xiao, S. & Schiffbauer, J. D. in *From Fossils to Astrobiology* 89-117 (Springer,
1222 2009).
- 1223 117 Astrop, T. I., Sahni, V., Blackledge, T. A. & Stark, A. Y. Mechanical properties
1224 of the chitin-calcium-phosphate “clam shrimp” carapace (Branchiopoda:
1225 Spinicaudata): implications for taphonomy and fossilization. *Journal of*
1226 *Crustacean Biology* **35**, 123-131 (2015).
- 1227 118 Chandran, R., Williams, L., Hung, A., Nowlin, K. & LaJeunesse, D. SEM
1228 characterization of anatomical variation in chitin organization in insect and
1229 arthropod cuticles. *Micron* **82**, 74-85 (2016).
- 1230 119 Horton, J. M. & Summers, A. P. The material properties of acellular bone in a
1231 teleost fish. *Journal of Experimental Biology* **212**, 1413-1420 (2009).
- 1232 120 Sibert, E. C. & Norris, R. D. New Age of Fishes initiated by the Cretaceous–
1233 Paleogene mass extinction. *Proceedings of the National Academy of Sciences* **112**,
1234 8537-8542 (2015).
- 1235 121 Alfaro, M. E. *et al.* Explosive diversification of marine fishes at the Cretaceous–
1236 Palaeogene boundary. *Nature Ecology & Evolution* **2**, 688 (2018).
- 1237 122 Friedman, M. Ecomorphological selectivity among marine teleost fishes during
1238 the end-Cretaceous extinction. *Proceedings of the National Academy of Sciences*
1239 **106**, 5218-5223 (2009).

1240 123 Sibert, E. C., Hull, P. M. & Norris, R. D. Resilience of Pacific pelagic fish across
1241 the Cretaceous/Palaeogene mass extinction. *Nature Geoscience* **7**, 667 (2014).
1242 124 Forchhammer, G. *Om de geognostiske forhold i en deel af Sjælland og naboøerne.*
1243 (1825).
1244 125 DePalma, R. A. *et al.* A seismically induced onshore surge deposit at the KPg
1245 boundary, North Dakota. *Proceedings of the National Academy of Sciences* **116**,
1246 8190-8199 (2019).
1247 126 Hiatt, E. E., Pufahl, P. K. & Edwards, C. T. Sedimentary phosphate and
1248 associated fossil bacteria in a Paleoproterozoic tidal flat in the 1.85 Ga
1249 Michigamme Formation, Michigan, USA. *Sedimentary Geology* **319**, 24-39
1250 (2015).
1251 127 Emanuel, K. A., Speer, K., Rotunno, R., Srivastava, R. & Molina, M. Hypercanes:
1252 A possible link in global extinction scenarios. *Journal of Geophysical Research:*
1253 *Atmospheres* **100**, 13755-13765 (1995).
1254 128 Covey, C., Thompson, S. L., Weissman, P. R. & MacCracken, M. C. Global
1255 climatic effects of atmospheric dust from an asteroid or comet impact on Earth.
1256 *Global and Planetary Change* **9**, 263-273 (1994).
1257 129 Crosby, C. H. & Bailey, J. The role of microbes in the formation of modern and
1258 ancient phosphatic mineral deposits. *Frontiers in Microbiology* **3**, 241 (2012).
1259 130 Zachos, J. C., Arthur, M. A. & Dean, W. E. Geochemical evidence for
1260 suppression of pelagic marine productivity at the Cretaceous/Tertiary boundary.
1261 *Nature* **337**, 61 (1989).
1262 131 Bucher, K. & Stober, I. Fluids in the upper continental crust. *Geofluids* **10**, 241-
1263 253 (2010).
1264 132 Kim, S.-T. & O'Neil, J. R. Equilibrium and nonequilibrium oxygen isotope effects
1265 in synthetic carbonates. *Geochimica et Cosmochimica Acta* **61**, 3461-3475 (1997).
1266 133 Petersen, S. *et al.* Effects of Improved ^{17}O Correction on Inter - Laboratory
1267 Agreement in Clumped Isotope Calibrations, Estimates of Mineral - Specific
1268 Offsets, and Temperature Dependence of Acid Digestion Fractionation.
1269 *Geochemistry, Geophysics, Geosystems* (2019).
1270 134 Hollund, H. I., Blank, M. & Sjögren, K.-G. Dead and buried? Variation in post-
1271 mortem histories revealed through histotaphonomic characterisation of human
1272 bone from megalithic graves in Sweden. *PloS One* **13**, e0204662 (2018).
1273 135 Passey, B. H. *et al.* Triple oxygen isotopes in biogenic and sedimentary
1274 carbonates. *Geochimica et Cosmochimica Acta* **141**, 1-25 (2014).
1275 136 Luz, B. & Barkan, E. Variations of $^{17}\text{O}/^{16}\text{O}$ and $^{18}\text{O}/^{16}\text{O}$ in meteoric waters.
1276 *Geochimica et Cosmochimica Acta* **74**, 6276-6286 (2010).
1277
1278
1279
1280

1281 **Figure Captions**

1282

1283 Figure 1. Photograph of the uppermost suevite (Unit 2A), transitional unit (Unit 1G) and
1284 green marlstone (transition between Units 1G and 1F) and Danian pelagic limestone (Unit
1285 1F) (units after Gulick et al., 2017⁴⁰) in Core 40R-1, and backscatter (BSE) images showing
1286 origin of micrite (core photo shows the location of samples). Depositional environment
1287 after Gulick et al. (2019)¹³ and Whalen et al. (in review)⁴². Pl. 1, 2. Foraminiferal calcite
1288 (white arrow) with a small amount of silicate melt (black arrows), 32-34 cm (616.56–
1289 616.48 mbsf); Pl. 3-7 micrite derived from decarbonation-carbonation (more angular
1290 grains); black arrows in Pl. 7 are clay; Pl. 3. 50-55 cm (616.74–616.79 mbsf), Pl. 4. 84-89
1291 cm (617.08–617.13 mbsf), Pl. 5. 100-104 cm (617.24–617.28 mbsf), Pl. 6. 104-105 cm
1292 (617.28–617.29 mbsf), Pl. 8-12. Micrite largely derived from melt (rounded grain shown
1293 with arrow in Pl. 11) along with silicate melt (white arrows in Pl. 9, 10), altered silicate
1294 melt (black arrow in Pl. 10), and mixed carbonate-silicate ash (arrow in Pl. 12), Pl. 7-11.
1295 108-110 cm (617.32–617.34 mbsf), Pl. 12. 110-118 cm (617.34–617.42 mbsf). Scale bars
1296 50 µm.

1297

1298 Figure 2. Stratigraphy of uppermost suevite (Unit 2A), transitional unit (Unit 1G) and green
1299 marlstone (Units 1G/1F transition) and Danian pelagic limestone (Unit 1F) (units after
1300 Gulick et al., 2017⁴⁰) in Core 40R-1. Planktic foraminiferal Zones after Lowery et al.
1301 (2018)⁴¹; He-isotopes after Lowery et al. (2018)⁴¹ and data herein; counts of charcoal grains
1302 after Gulick et al. (2019)¹³. Small grey drops indicate occurrence of melt droplets.

1303

1304 Figure 3. Thin section views of important features in the uppermost suevite, transitional
1305 unit and green marlstone. Pl. 1, 2. Upper pyritized charocal layers in green marlstone. Pl.
1306 1. Cross polarized light (white arrows show apparent bedforms; blue arrows show
1307 foraminiferal lags, see Discussion); Pl. 2. Reflected light (white arrows show apparent
1308 bedforms; see Discussion). Pl. 3, 4. Images showing clay seams and possible algal mats (as
1309 shown by green epifluorescence (shown by arrows in Pl. 4, see Discussion)); Pl. 3. Cross-
1310 polarized light-Epifluorescence; Pl. 4. Epifluorescence. Pl. 5, 6. Pyrite layers cross-
1311 polarized light. Pl. 7. Fluid escape structure with vein (shown with arrow). Pl. 8 Alternating
1312 interval of melt rich (base and top) and carbonate rich (middle) suevite. Samples all in Core
1313 40R-1: Pl. 1, 2. 31-32 cm (616.54–616.56 mbsf); Pl. 3, 4. 33.5-34.5 cm (616.575–616.585
1314 mbsf); Pl. 5. 100-104 cm (617.24–617.28 mbsf); Pl. 6. 104-105 cm (617.28–617.29 mbsf);
1315 Pl. 7. 106-108 cm (617.30–617.32 mbsf); Pl. 8. 108-110 cm (617.32–617.34 mbsf). Scale
1316 bars represent 2 mm.

1317

1318 Figure 4. Backscattered electron (BSE) and secondary electron images of pyrite and
1319 petrified wood from the lower transitional unit and green marlstone. Pl. 1, 2. Pyrite shards
1320 preserving wood structure (arrows); Pl. 3. Pyrite showing wood structure (arrow). Pl. 4, 5.
1321 Pyrite showing more (left) and less (right) pyritized areas with wood structure (right); Pl.
1322 5 is close up view of the boundary between the two areas in Pl. 4. Pl. 6. Area of pyrite
1323 showing organic structure. Pl. 7, 8. Pyrite containing dark carbon needles (possible conifer
1324 needles). Pl. 9. Dolomite (shown by arrow as identified in EDS) underlying pyrite grain.
1325 Pl. 10-12. Petrified wood. Samples all in Core 40R-1: Pl. 1, 2. 31-32 cm (616.55–616.56
1326 mbsf); Pl. 3. 100-104 cm (617.24–617.28 mbsf); Pl. 4-6. 32-34 cm (616.56–616.58 mbsf);

1327 Pl. 7, 8. 100-104 cm (617.24–617.28 mbsf); Pl. 9. 32-34 cm (616.56–616.58 mbsf); Pl. 10-
1328 12. 31cm (616.55 mbsf). Pl. 1-9. BSE images of thin sections; Pl. 10-12 secondary electron
1329 images of strewn slides. Scale bars represent 5 μ m.

1330

1331 Figure 5. Strontium, carbon, oxygen and clumped isotope data from the uppermost suevite
1332 (unit 2A), transitional unit (1G), the 1G/1F transition (tr., which contains the green
1333 marlstone at its base), and pelagic limestone (1F). Interval of soft-sediment deformation is
1334 shown by the horizontal gray shaded area as is interval of highest Ir enrichment after
1335 Goderis et al. (2019)⁴³. Sr isotope values are from HCl leaches. The $\delta^{18}\text{O}$ temperatures are
1336 calculated from $\delta^{18}\text{O}_{\text{occ}}$ values using the relation of Kim & O'Neil (1997)¹³², assuming a
1337 seawater $\delta^{18}\text{O}$ value of -1‰. Clumped isotope temperatures are calculated from Δ_{47} values
1338 following Petersen et al. (2019)¹³³. Error bars for clumped isotopes are 95% confidence
1339 intervals, and smaller symbols denote samples that were not analyzed in replicate. Gray
1340 vertical bars indicate mean temperature values ($\pm 1\sigma$) for the pelagic limestone (1F), the
1341 transitional unit (excluding the interval marked tr.), and the uppermost suevite (2A). Range
1342 of Sr isotope values for K-Pg sections⁶¹ is shown. Occurrences of hydrothermal ZnS and
1343 pyrite and apatite and evaporite are indicated.

1344

1345 Figure 6. Backscattered electron (BSE) of apatite from the green marlstone including
1346 ancient and modern forms used for comparison. Pl. 1, 2, 3. Clusters of spherical fossil
1347 bacteria that resembles coprolites, Pl. 2 is close up of Pl. 1. Pl. 5-7. Piece of bone tunneled
1348 by cyanobacteria; Pl. 5. Whole object; Pl. 6, 7. Close up views of Pl. 5. Note calcite growing
1349 in pores in 7 (examples shown by arrow). Pl. 9-12. Layered and hooked specimens of
1350 possible marine arthropods. Pl. 13-16: possible small fish fossil. Samples all in Core 40R-
1351 1, 32-34cm. Pl. 1-7, 9-12. BSE images of thin sections. Pl. 4. Encrusted bacterial cells in
1352 hyaena coprolite from Pesquero et al. 2017¹⁰⁶ (Figure 4C) (image available via a Creative
1353 Commons Attribution License (CC BY)). Pl. 8. Brightfield reflected light image of section
1354 of an altered human bone tunneled by cyanobacteria from Hollund et al. 2018¹³⁴ (Figure
1355 6C) (image available via a Creative Commons Attribution License (CC BY)). Scale bars on
1356 individual images.

1357

1358 Figure 7. Transmission Electron Microscope (TEM) and secondary electron images
1359 showing ultrastructure of calcite in the transitional unit and comparison with calcite
1360 produced by thermal decarbonation; both classes of calcite shows planar features. Pl. 1-6
1361 are of TEM micrographs of calcite in Sample 40R-1, 91cm (617.13 mbsf). Pl. 7, 8 are of
1362 TEM micrographs of calcite in Sample 40R-1, 33cm (616.57 mbsf) with Moiré fringe
1363 areas shown with insets. Pl. 9 is SEM of calcite in fault zone produced by thermal
1364 decarbonation (from Cristiano Colletini pers. comm.). Pl. 10 is backscattered electron
1365 (BSE) of 40R-1, 72-76 cm (616.94–616.98 mbsf). Scale bars in individual images. Pl. 11,
1366 12 are SEMs of calcite produced by experimental thermal decarbonation from Rodriguez
1367 Navarro et al. (2009)⁵⁴. Images used with permission from the Mineralogical Society of
1368 America.

1369

1370 Figure 8. (A). Apparent seawater $\delta^{18}\text{O}$ versus clumped isotope temperature, contoured for
1371 constant $\delta^{18}\text{O}_{\text{occ}}$ (thin gray lines). The apparent seawater $\delta^{18}\text{O}$ values are calculated using
1372 the oxygen isotope thermometer of Kim and O'Neil (1997)¹³², with temperatures based on

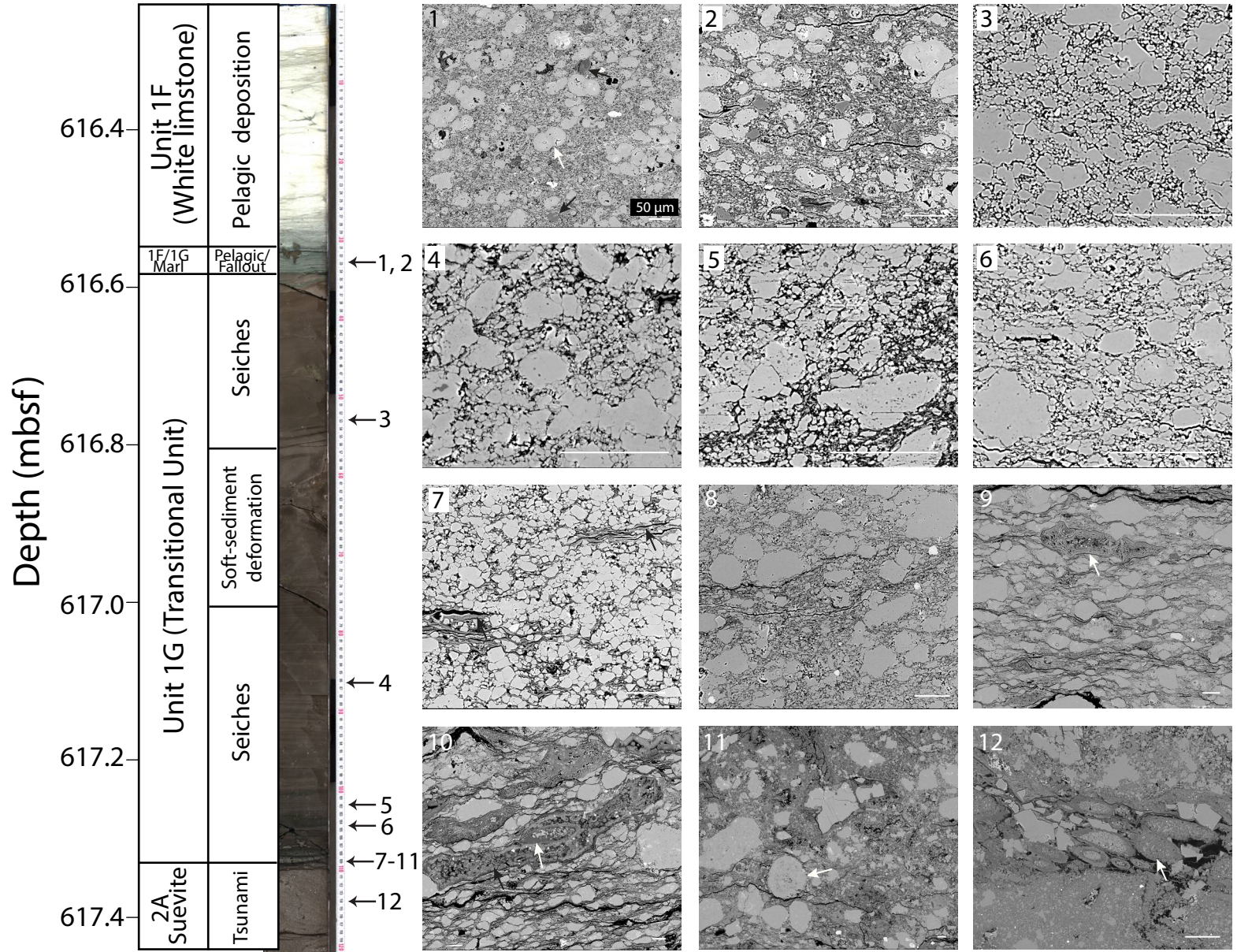
1373 clumped isotopes. The color scale indicates the traditional oxygen isotope-based
1374 temperatures under the assumption that $\delta^{18}\text{O}_w = -1\%$. (B) Illustration of the scenario where
1375 the initial carbonate forms in cooler (but still extremely warm) seawater with $\delta^{18}\text{O} = -1\%$
1376 (white symbols), and subsequently recrystallizes on the higher-temperature seafloor under
1377 rock-buffered ($\delta^{18}\text{O}$ -preserving) conditions (black arrows). Such recrystallization results
1378 in increased clumped isotope temperatures but little or no change in $\delta^{18}\text{O}_{\text{occ}}$, which results
1379 in apparent seawater $\delta^{18}\text{O}$ values that are erroneously high.

1380
1381 Figure 9. Backscattered electron (BSE) and secondary electron images of anydrite, halite,
1382 apatite, ZnS and pyrite from the transitional unit and green marlstone. Pl. 1, 4, 6. Halite.
1383 Pl. 2, 3, 5. Anhydrite. Pl. 7. Apatite (arrow) in chlorite vein. Pl. 8 and 9. Apatite (arrows)
1384 surrounded by halite. Pl. 10-11 ZnS (light grey) with calcite (dark grey shown by arrow)
1385 crystals inside. Pl. 12, Pyrite crystals (upper arrow) in chlorite (lower arrow) vein. Samples
1386 all in Core 40R-1: Pl. 1, 4, 6, 31 cm (616.55 mbsf); Pl. 2, 3, 5. 108 cm (617.32 mbsf); Pl.
1387 7, 12. 106-108 cm (617.30–617.32 mbsf). Pl. 8, 9. 110 cm (617.34 mbsf); Pl. 10, 11. 67-
1388 72cm (616.91–616.96 mbsf); Pl. 7, 10-12. BSE images of thin sections; Pl. 1-6, 8, 9
1389 secondary electron images of strewn slides. Scale bars on individual images.

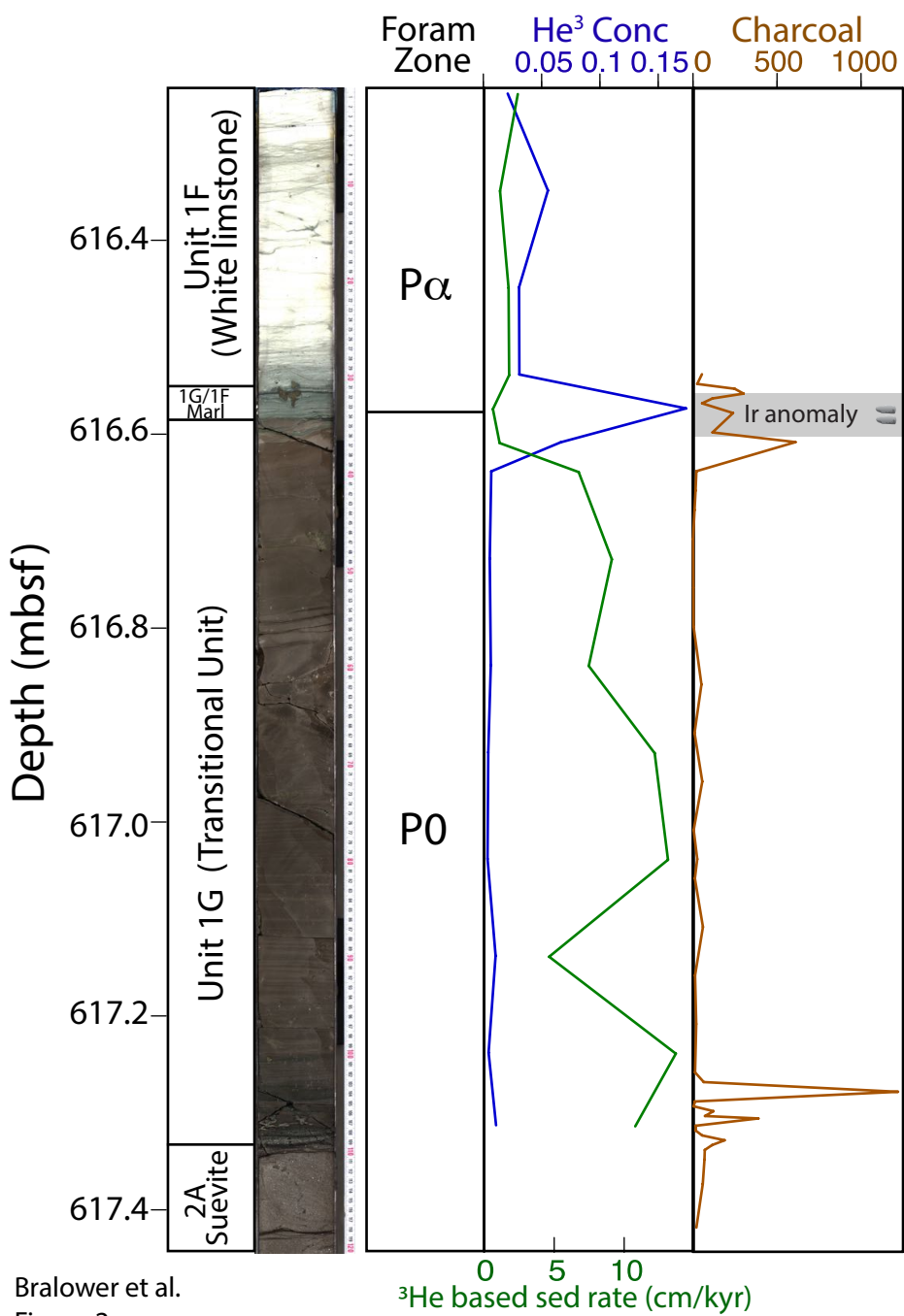
1390
1391 Figure 10. Cartoon showing proposed origin of the transitional unit and green marlstone.
1392 Panel A Upper row -- deposition of transitional unit showing cross section (left) and birds-
1393 eye view (right). Red arrows in section indicate convection from central melt sheet; thick
1394 black arrows show direction of seiche wave transport and deposition of CaCO_3 in
1395 transitional unit at Site M0077; location of Site M0077 indicated by green arrow. Birds-
1396 eye view shows whole crater with opening to the Gulf of Mexico to the northeast and
1397 morphological features including the peak ring; seiche waves indicated by double ended
1398 arrows; tsunami waves by single arrows. Location of M0077 and Yax-1 indicated by red
1399 symbols; green line indicates section in Panel A. Site water depth after Lowery et al.
1400 (2018)⁴¹. Panel B Lower row – deposition of green marlstone at Site M0077 showing
1401 atmospheric fallout combined with eutrophic conditions.

1402
1403 Figure 11. Recovery of life and its relationship with environment in the nascent crater. At
1404 left is sediment core showing lowermost and uppermost transitional unit and green
1405 marlstone and its environmental interpretation. At right are fossil occurrences at various
1406 trophic levels and timing of the recovery. Higher orders include apatite remains of small
1407 fish and pelagic crustaceans. Planktonic protists are represented by planktic
1408 foraminifera, calcareous nannoplankton and dinoflagellates. Microcrystals that appear to be
1409 made by cyanobacteria⁴⁴. Scale bars by individual images (bars by *Z. sigmoides* pertains to
1410 four nannofossil images).

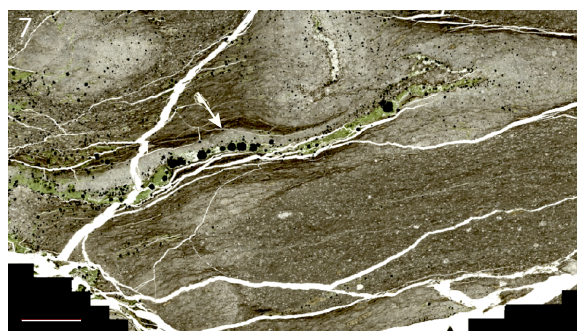
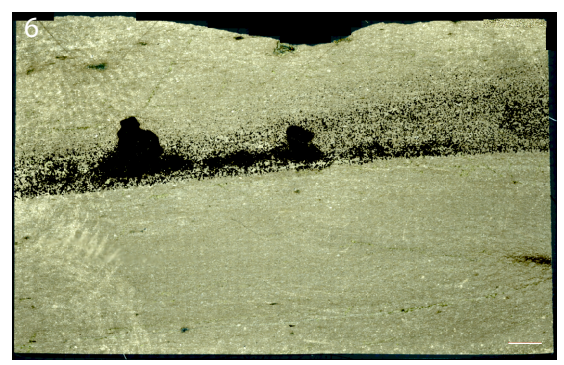
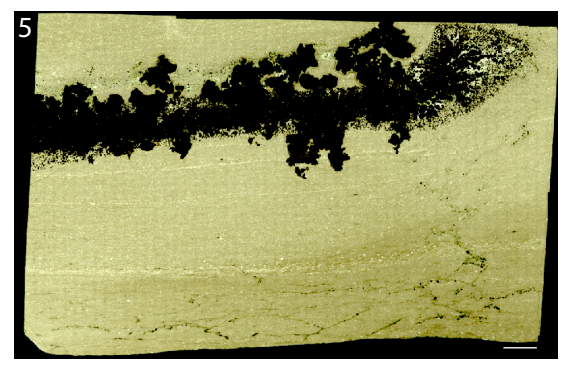
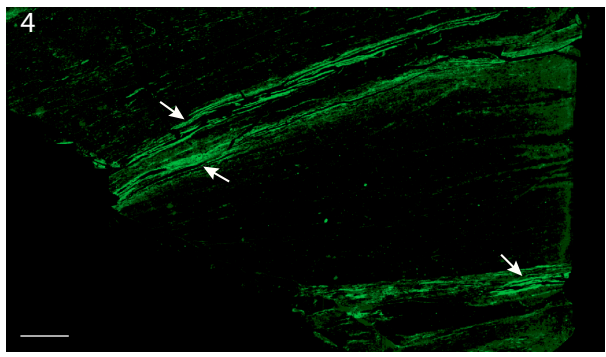
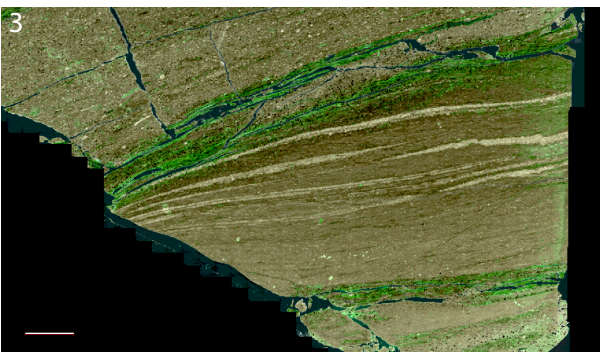
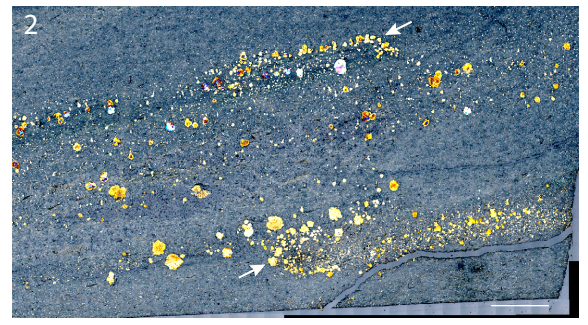
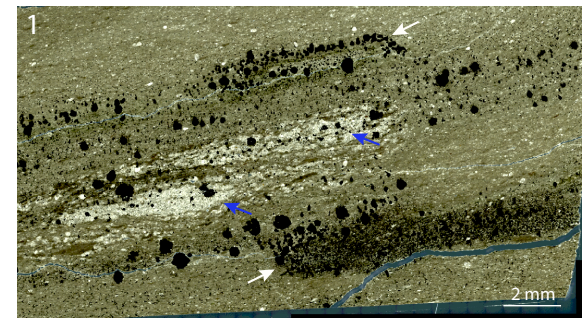
1411
1412
1413



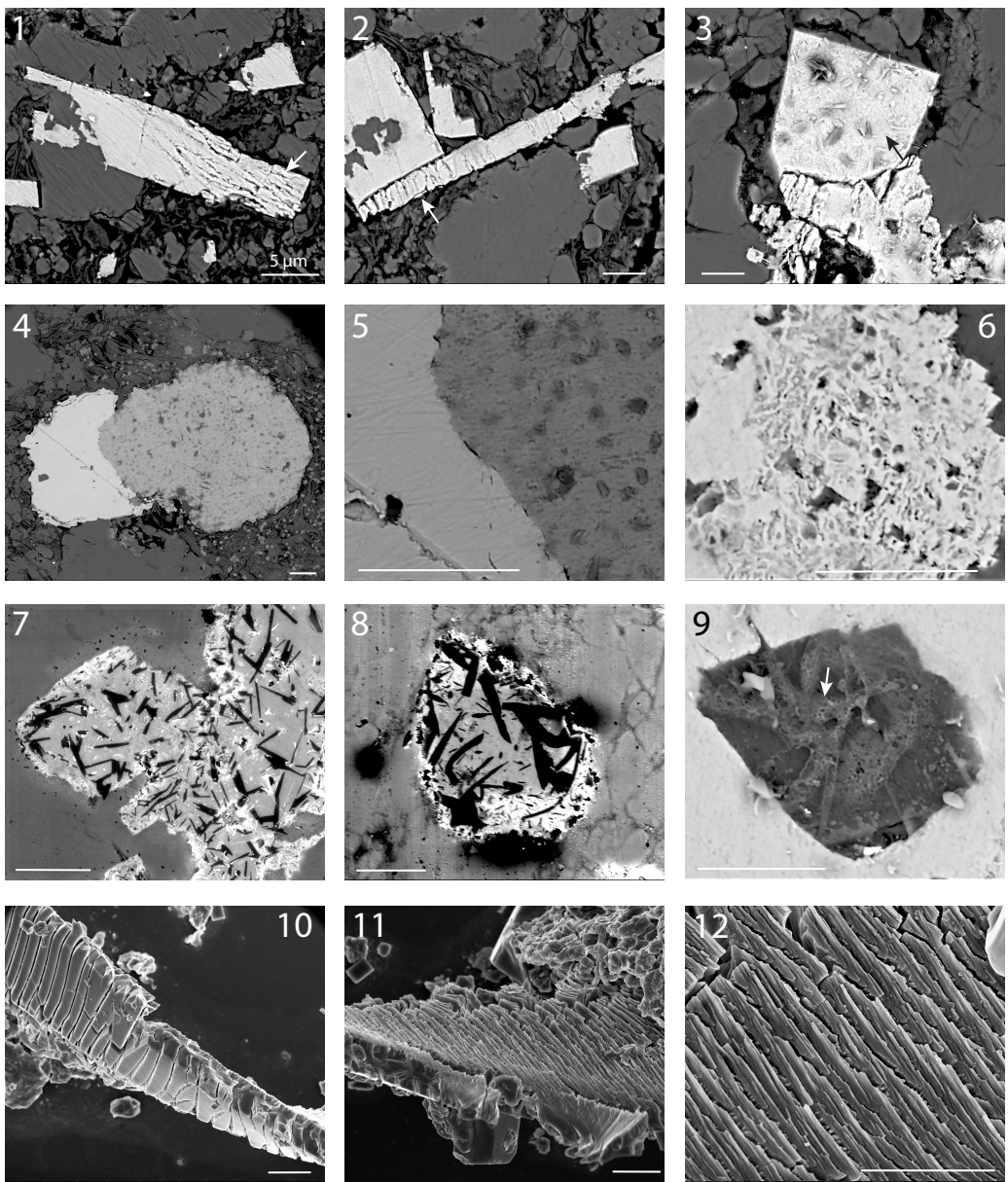
Bralower et al.
Figure 1



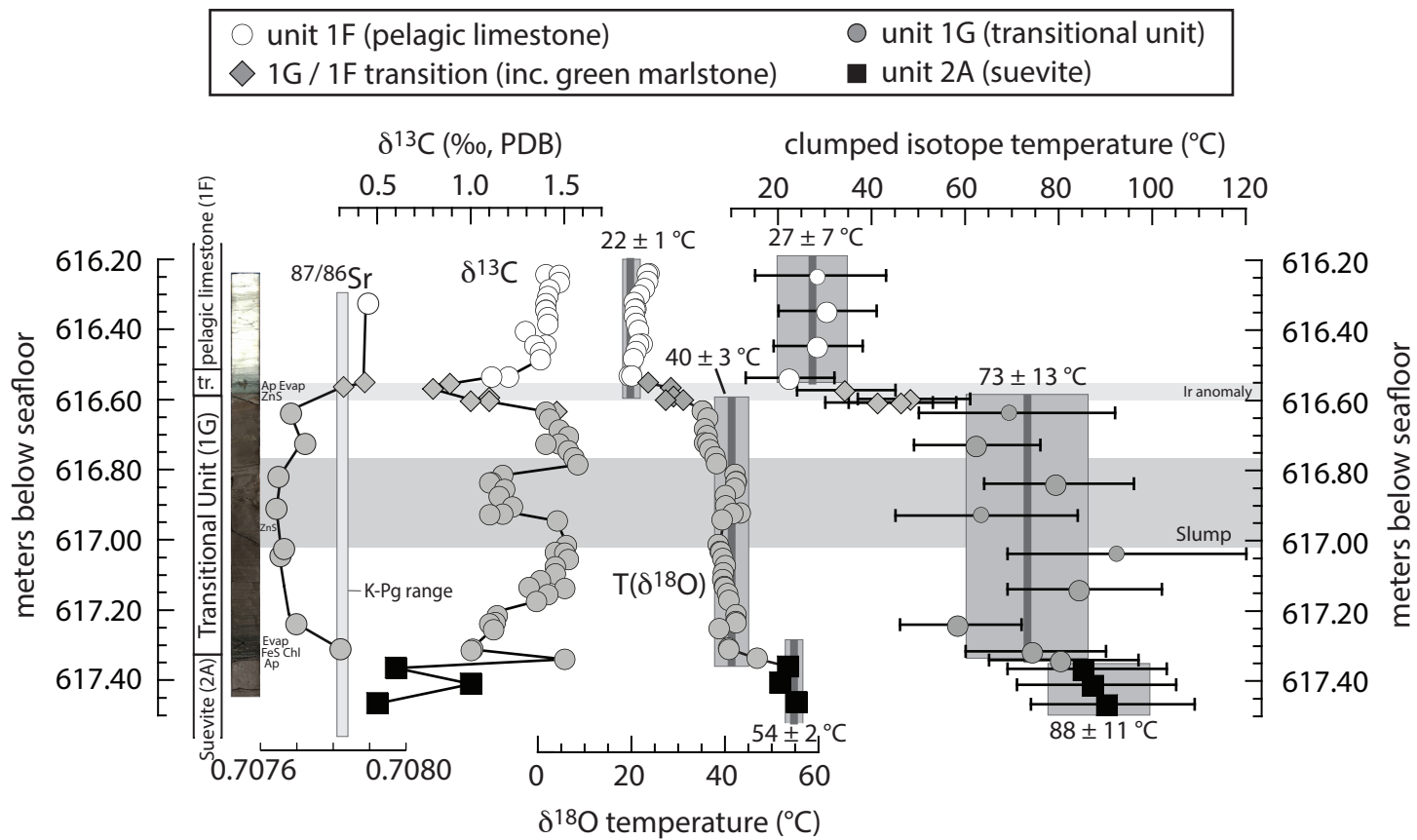
Bralower et al.
Figure 2



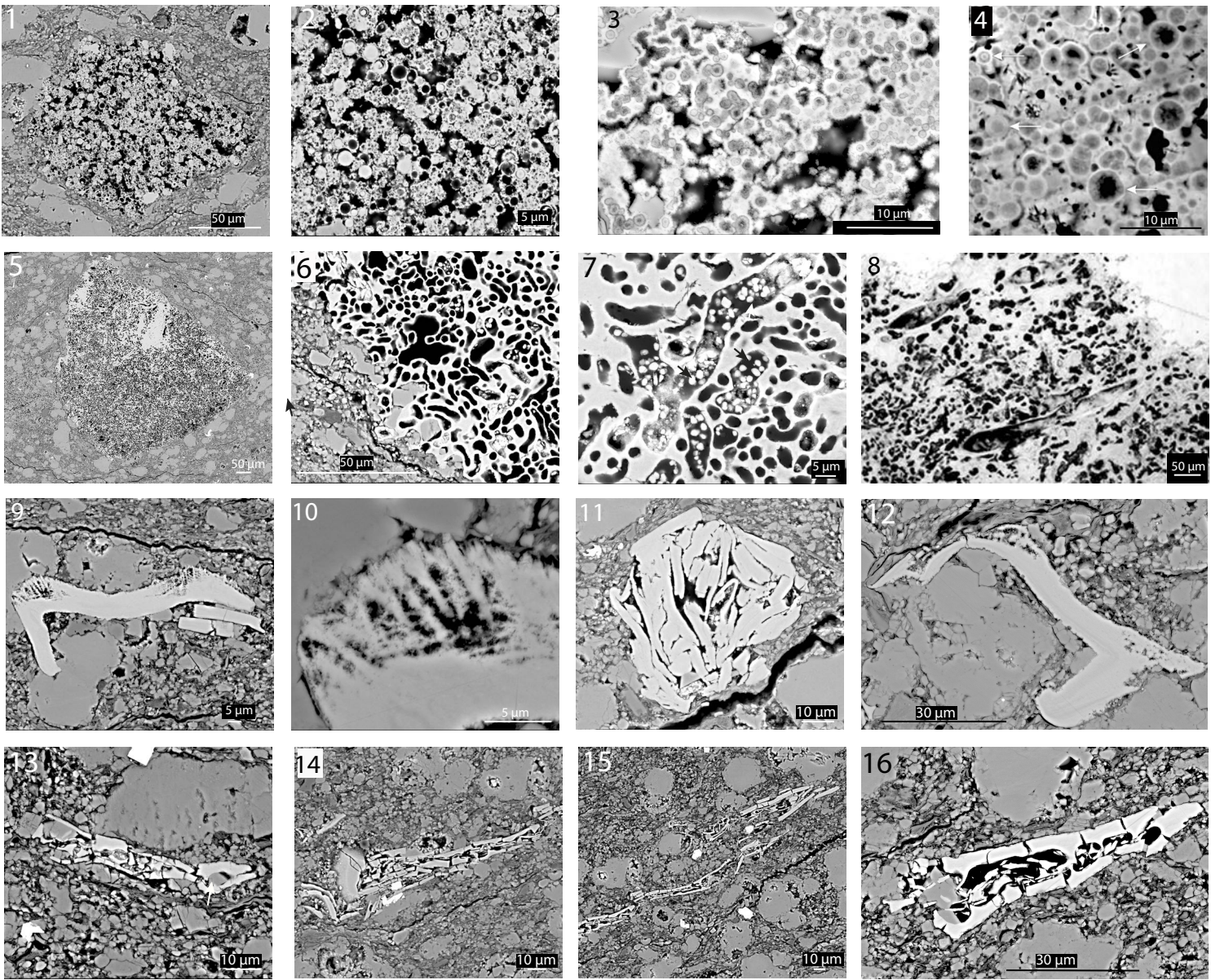
Bralower et al.
Figure 3



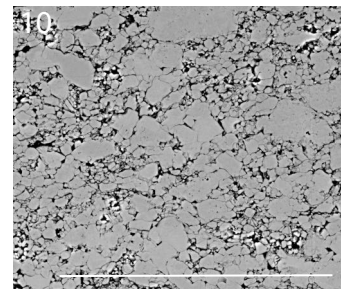
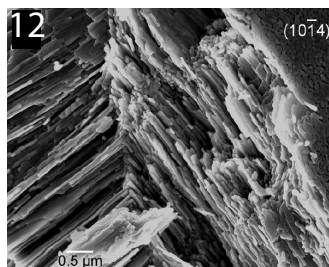
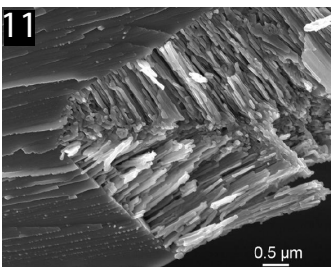
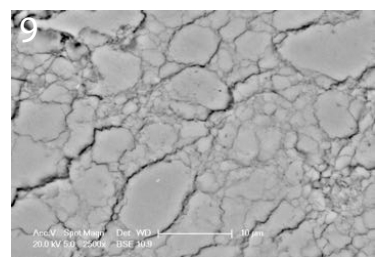
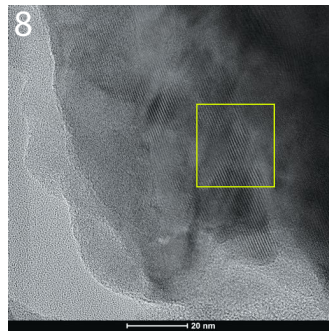
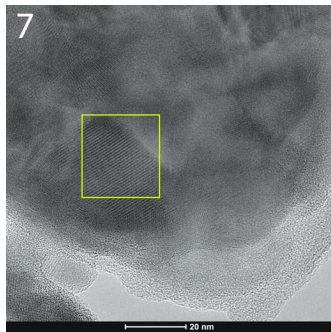
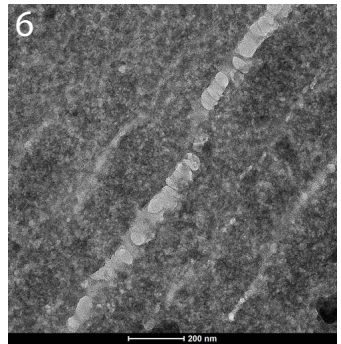
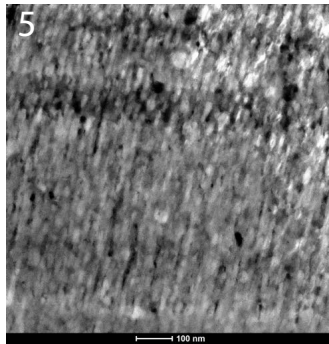
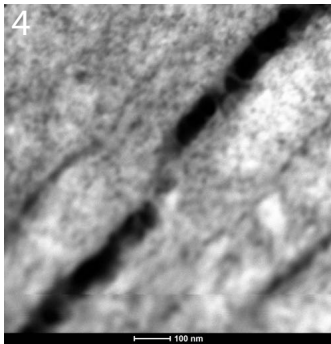
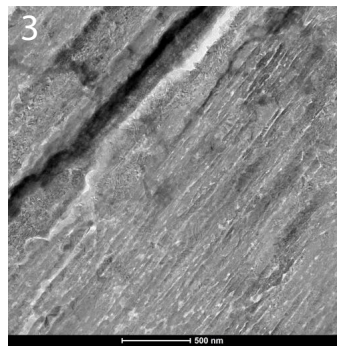
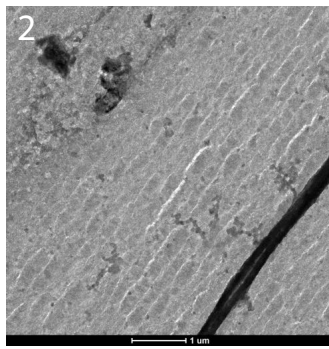
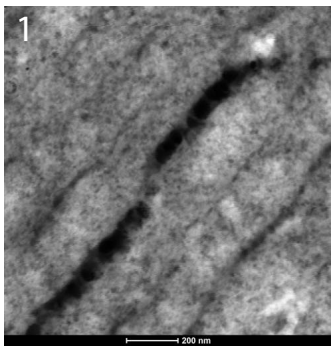
Bralower et al.
Figure 4



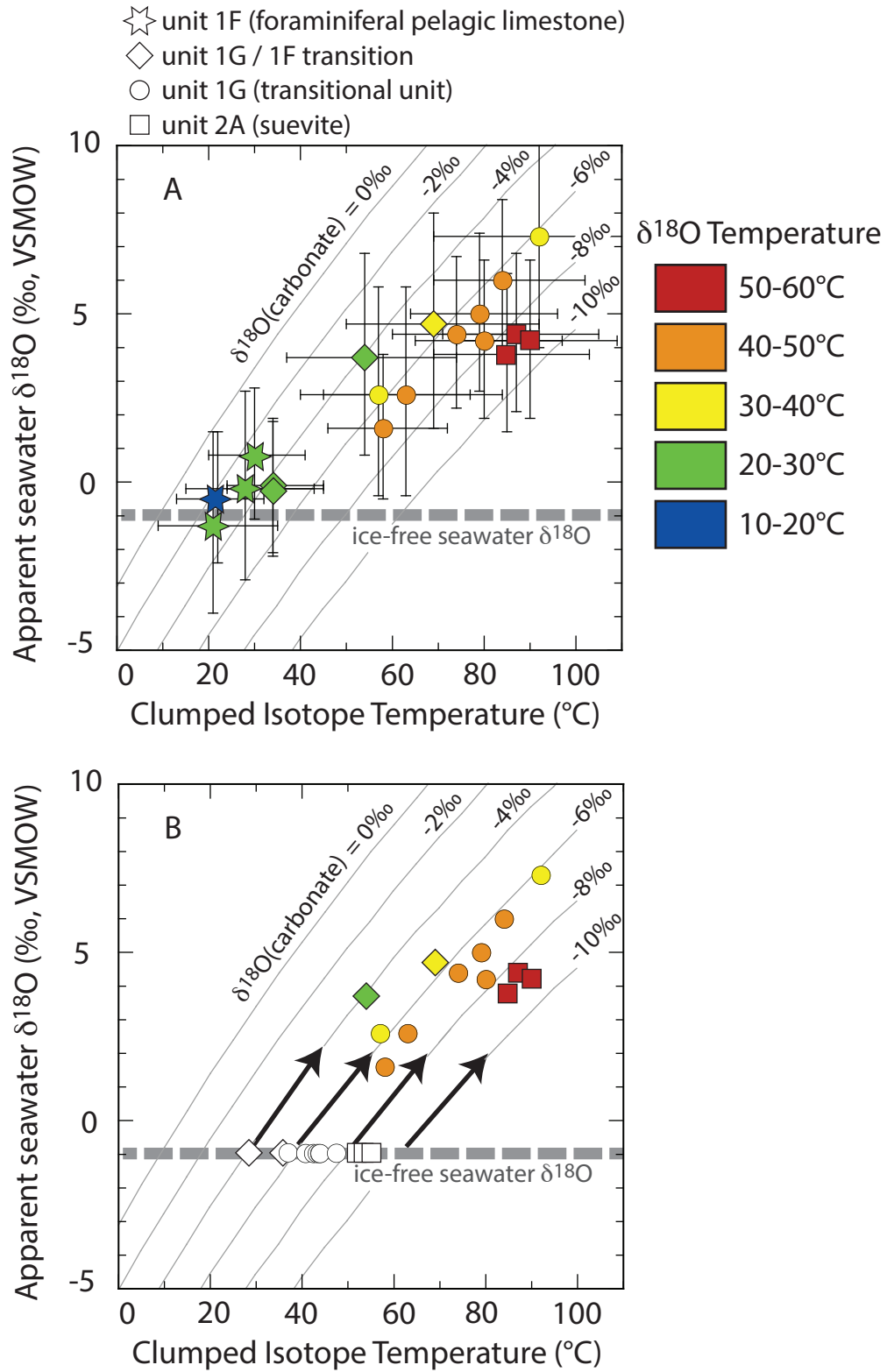
Bralower et al.
Figure 5



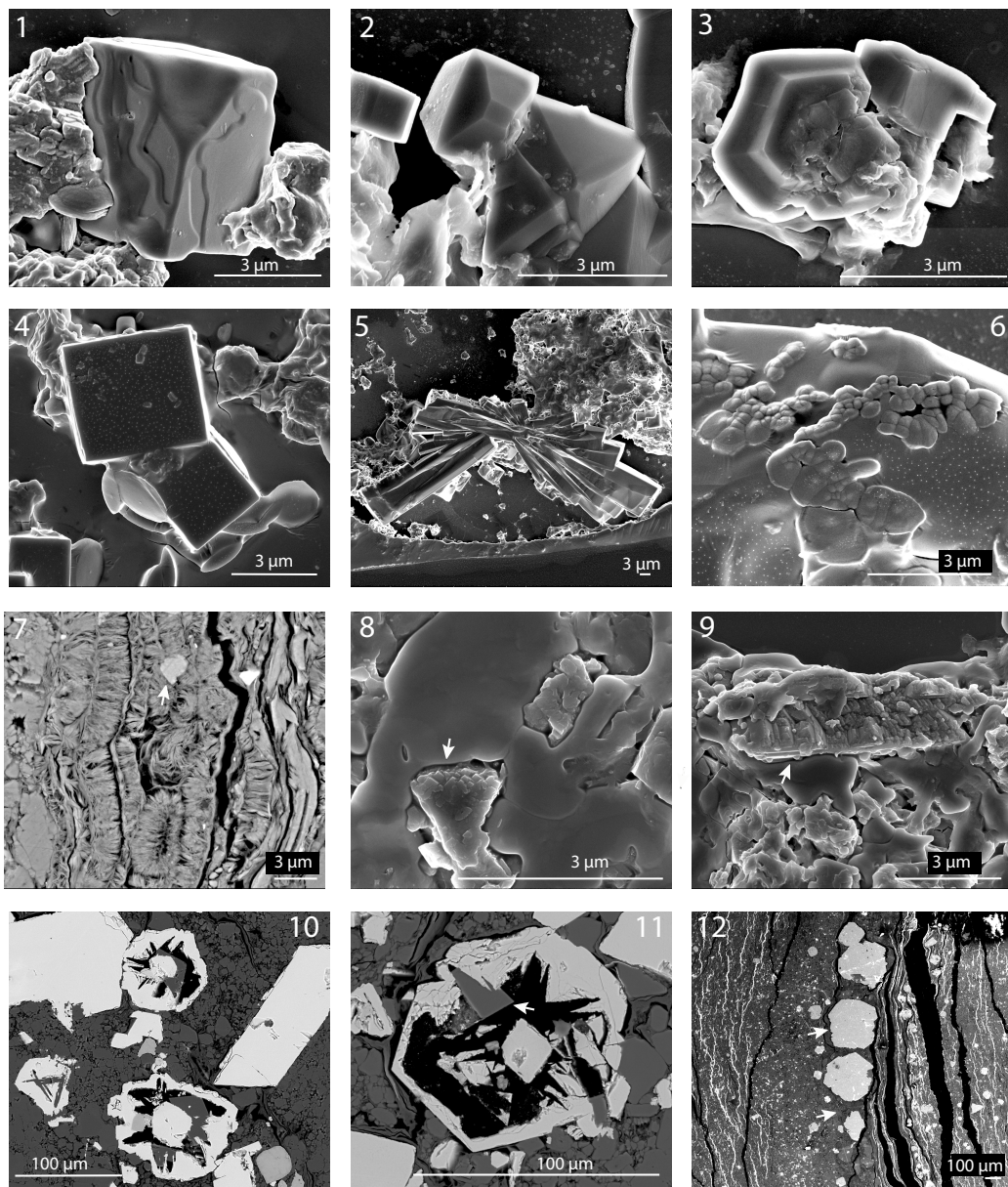
Bralower et al.
Figure 6



Bralower et al.
Figure 7

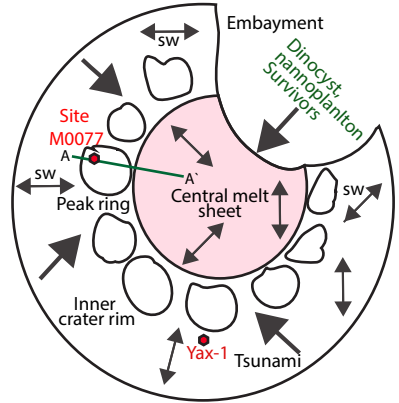
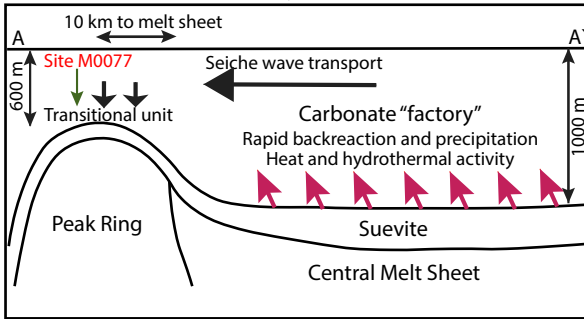


Bralower et al.,
Figure 8

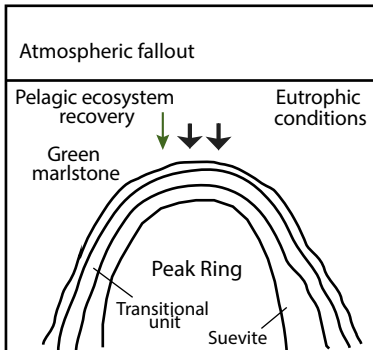


Bralower et al.
Figure 9

A. Transitional Unit time Carbonate "factory"



B. Green marlstone time Fall out and environmental recovery



Sedimentology

Possible Environmental Interpretation

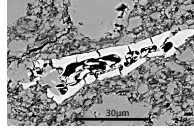
Recovery of life Years to millennia

mbsf

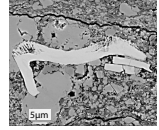
Upper Trans. Unit
green marlstone



Small fish



Crustacean



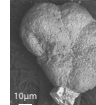
616.55

Darkness,
Stratospheric
fallout of charcoal
Eutrophication

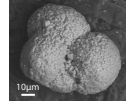
Planktonic protista



Cervistiella



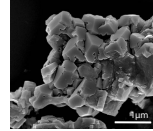
P. eugubina



G. globoconusa

616.60

Microbes

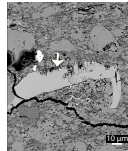


Lower Trans. Unit
upper Suevite

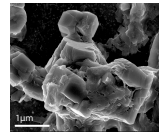


Hours to days

Crustacean



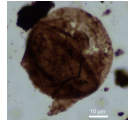
Microbes



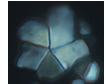
617.30

Blast wave charcoal
Seiche wave

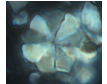
Planktonic protista



T. evittii



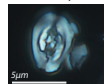
Braarudosphaera



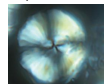
B. sparsus

617.35

Rim-wave tsunami



Z. sigmoides



C. reinhardtii